SIAM J. SCI. COMPUT.
Vol. 41, No. 4, pp. A2088–A2116

PLANEWAVE DENSITY INTERPOLATION METHODS FOR 3D HELMHOLTZ BOUNDARY INTEGRAL EQUATIONS*

CARLOS PÉREZ-ARANCIBIA†, CATALIN TURC‡, AND LUIZ FARIA§

Abstract. This paper introduces planewave density interpolation methods for the regularization of weakly singular, strongly singular, hypersingular, and nearly singular integral kernels present in 3D Helmholtz surface layer potentials and associated integral operators. Relying on Green's third identity and pointwise interpolation of density functions in the form of planewaves, these methods allow layer potentials and integral operators to be expressed in terms of integrand functions that remain bounded or even more regular regardless of the location of the target point relative to the surface sources. Common challenging integrals that arise in both Nyström and boundary element discretization of boundary integral equations can then be numerically evaluated by standard quadrature rules irrespective of the kernel singularity. Closed-form and purely numerical planewave density interpolation procedures are presented in this paper, which are used in conjunction with Chebyshev-based Nyström and Galerkin boundary element methods. A variety of numerical examples, including problems of acoustic scattering involving multiple touching and even intersecting obstacles, demonstrate the capabilities of the proposed technique.

Key words. Helmholtz equation, integral equations, Nyström methods, boundary element methods

AMS subject classifications. 45A05, 45E99, 30E25, 65R20

DOI. 10.1137/19M1239866

1. Introduction.

Challenging weakly singular, strongly singular, hypersingular, and nearly singular surface integrals are ubiquitous to boundary integral equation (BIE) formulations of linear partial differential equations (PDEs). A plethora of numerical and semianalytical procedures including, for instance, singularity subtraction[1] [7, 17, 22, 23, 40, 41], Duffy-like transformations [14, 20, 31, 33, 34], polar singularity cancelation [5, 21, 36], and singularity extraction [35, 37], among other techniques, have been proposed in the literature for the evaluation of these difficult integrals in the context of both Nyström methods and boundary element methods (BEMs). Despite all these significant efforts and the compelling advantages that BIE methods offer over standard volume discretization techniques such as finite element and finite difference methods—especially in handling unbounded domains and seamlessly incorporating radiation conditions at infinity for time-harmonic wave scattering—they still face criticism for being difficult to implement. From the authors' viewpoint, the main source of practical difficulties arises from the significant effort researchers and practitioners have to invest into understanding and implementing a specific set of techniques tailored to handle the various integration scenarios concerning the target point location relative to the surface sources. We hereby ad-

*Submitted to the journal's Methods and Algorithms for Scientific Computing section January 22, 2019; accepted for publication (in revised form) May 9, 2019; published electronically July 2, 2019.
https://doi.org/10.1137/19M1239866
Funding: This work was supported by FONDECYT grant 11181032.

†Institute for Mathematical and Computational Engineering, School of Engineering and Faculty of Mathematics, Pontificia Universidad Católica de Chile, Santiago, Region Metropolitana, 7820436, Chile (cperez@mat.puc.cl, http://cperezar.sitios.ing.uc.cl/).
‡Department of Mathematical Sciences, New Jersey Institute of Technology, Newark, NJ 07102 (catalin.c.turc@njit.edu).
§Laboratoire POEMS, INRIA, 91762 Palaiseau Cedex, France (luiz.maltez-faria@inria.fr).

[1] This technique has also been referred to as singularity extraction by some authors.

dress this issue for both Nyström and Galerkin boundary element discretizations of 3D Helmholtz BIEs by introducing a universal semianalytical procedure capable of regularizing all the aforementioned challenging surface integrals at the continuous level, i.e., prior to numerical integration. For the sake of conciseness, we specifically consider combined-field BIE formulations of sound-soft (Dirichlet) and sound-hard (Neumann) scattering problems leading to the well-known Brakhage–Werner [3] and Burton–Miller [6] integral equations, respectively, which feature all four boundary integral operators of Calderón calculus.

As mentioned above, there is extensive literature on the subject. We refer the reader to [30] for a thorough review concerning Nyström methods and various approaches to dealing with nearly singular integrals. Regarding BEMs specifically, two main groups of techniques can be distinguished. On one hand, we have semianalytical techniques [7, 17, 22, 23, 40, 41] whereby singular terms are extracted from the kernel to be integrated in closed form, while the remaining smoother part is integrated numerically by means of standard quadrature rules. And, on the other hand, we have techniques based on regularizing coordinate transformations [14, 20, 21, 31, 33, 34, 36] whereby specialized changes of variables are utilized to turn singular integrands into regular (analytic) integrands to which standard quadrature rules can be directly applied to achieve any desired accuracy. Although effective at dealing with the specific classes of integrands (on polygonal surface meshes) and basis functions for which they have been designed, none of the aforementioned techniques handles nearly singular integrals arising when target points lying off the surface are close to the surface sources.

In detail, this paper presents planewave density interpolation (PWDI) methods for the regularization of weakly singular, strongly singular, hypersingular, and nearly singular integral kernels present in Helmholtz layer potentials and the associated boundary integral operators. Relying on Green's third identity and a certain Taylor-like interpolation of the surface density in terms of homogeneous solutions of the underlaying PDE (planewaves in this case), density interpolation methods [29, 30] allow layer potentials and operators to be expressed in terms of integrand functions that are smooth (at least bounded) regardless of the target point location. The resulting surface integrals can then be numerically evaluated by means of standard off-the-shelf quadrature rules irrespective of the singularity of the associated integral kernels. As such, kernel-regularized layer potentials and operators can be directly evaluated at target points that are arbitrarily close to their surface sources enabling, in particular, the straightforward Nyström or Galerkin BEM discretization of BIEs involving multiple obstacles that are close, touching, or even intersecting each other. Indeed, we demonstrate through numerical experiments that BIEs posed on the surface of composite obstacles, i.e., obstacles that can be expressed as unions of geometrically simpler intersecting obstacles, can be recast as BIEs posed on the union of the boundaries of the simpler domains, which, upon application of the proposed PWDI kernel-regularization technique, can be directly solved using the BEM retaining the expected order of convergence. This aspect of the proposed technique may significantly simplify the numerical solution of many real-world problems involving intricate obstacles, as it effectively allows bypassing the often involved task of meshing complex surfaces.

The PWDI method presented here is closely related to the boundary regularized integral equation formulation method (BRIEF) [24, 38, 39] and other low-order regularization techniques [25, 26] that rely on interpolation of the surface density function and Green's representation formula. In fact, the PWDI method can be viewed as an extension/generalization of BRIEF in the sense that the PWDI method can be applied

to all four boundary integral operators of Calderón calculus separately—including the challenging hypersingular operator—thus enabling its use in both direct and indirect BIE formulations free of spurious resonances. It can in principle produce surface integrands of any prescribed degree of smoothness, it can be used in conjunction with nonsmooth surface representations such as those produced by triangular mesh generators, and it can handle intersecting surfaces. At the continuous level, before any Nyström or Galerkin BEM discretization is utilized, BRIEF can be considered equivalent to the lowest-order version (with $M = 0$) of the PWDI method applied to the classical Dirichlet first-kind or Neumann second-kind direct BIEs given in terms of the single- and double-layer operators.

The structure of this paper is as follows: The theoretical basis of Taylor interpolation on regular surfaces, and of density interpolation methods in general, are established in section 3. Two PWDI procedures are next introduced in section 4. One amounts to the nontrivial extension to three dimensions of the low-order closed-form analytic procedure put forth in [29] (section 4.1), while the other is a purely numerical procedure for the construction of arbitrarily high-order planewave density interpolants (section 4.2). Section 5 then provides the details on the discretization of kernel-regularized layer potentials and integral operators by means of a Chebyshev-based Nyström method (section 5.1) and a Galerkin BEM (section 5.2). Section 6, finally, presents a variety of numerical examples that validate and demonstrate the various capabilities of the PWDI technique in the context of both Nyström methods and BEMs.

2. Preliminaries. For the sake of definiteness, we focus in this paper on scattering problems related to acoustic sound-soft and sound-hard scatterers, e.g., either Dirichlet or Neumann boundary conditions. We thus seek scattered fields that are solutions of the following exterior Dirichlet and Neumann boundary value problems:

$$\begin{cases} \Delta u_D^s + k^2 u_D^s = 0 & \text{in } \mathbb{R}^3 \setminus \Omega, \\ u_D^s + u^{\text{inc}} = 0 & \text{on } \Gamma, \\ \lim\limits_{|\boldsymbol{r}|\to\infty} |\boldsymbol{r}| \left(\dfrac{\partial u_D^s}{\partial |\boldsymbol{r}|} - \mathrm{i}k u_D^s \right) = 0 \end{cases} \tag{2.1}$$

and

$$\begin{cases} \Delta u_N^s + k^2 u_N^s = 0 & \text{in } \mathbb{R}^3 \setminus \Omega, \\ \dfrac{\partial u_N^s}{\partial \boldsymbol{n}} + \dfrac{\partial u^{\text{inc}}}{\partial \boldsymbol{n}} = 0 & \text{on } \Gamma, \\ \lim\limits_{|\boldsymbol{r}|\to\infty} |\boldsymbol{r}| \left(\dfrac{\partial u_N^s}{\partial |\boldsymbol{r}|} - \mathrm{i}k u_N^s \right) = 0, \end{cases} \tag{2.2}$$

respectively, where $\Omega \subset \mathbb{R}^3$ is a bounded obstacle whose boundary Γ is a piecewise smooth, oriented, and closed surface. (The incident fields u^{inc} in (2.1) and (2.2) are assumed to be solutions of the Helmholtz equation in all of $\mathbb{R}^3$.)

The Dirichlet (2.1) and Neumann (2.2) scattering problems can be formulated via well-posed BIEs by means of the combined field approach introduced by Brakhage and Werner [3] and Burton and Miller [6], respectively. The combined field approach relies on the use of Helmholtz single- and double-layer potentials, hereby denoted as

$$(\mathcal{S}\varphi)(\boldsymbol{r}) := \int_\Gamma G(\boldsymbol{r}, q)\varphi(q)\,\mathrm{d}s(q) \quad \text{and} \quad (\mathcal{D}\varphi)(\boldsymbol{r}) := \int_\Gamma \frac{\partial G(\boldsymbol{r}, q)}{\partial \mathbf{n}(q)}\varphi(q)\,\mathrm{d}s(q) \tag{2.3}$$

for $\boldsymbol{r} \in \mathbb{R}^3 \setminus \Gamma$, respectively, where $G(\boldsymbol{r}, \boldsymbol{r}') := (4\pi)^{-1} \mathrm{e}^{\mathrm{i}k|\boldsymbol{r}-\boldsymbol{r}'|}/|\boldsymbol{r}-\boldsymbol{r}'|$ is the outgoing free-space Green function for the Helmholtz equation in $\mathbb{R}^3$ with wavenumber $k > 0$. (In what follows, we utilize the symbol $\boldsymbol{r}$ to denote points that do not lie on the surface Γ, while the symbols p and q are used exclusively to refer to points on the surface Γ.)

Interior and exterior Dirichlet/Neumann traces of the single- and double-layer potentials give rise to the four boundary integral operators of Calderón calculus associated to the Helmholtz equation. Specifically, the Helmholtz single-layer (S), double-layer (K), adjoint double-layer (K'), and hypersingular (N) operators are defined as

(2.4)
$$(S\varphi)(p) := \int_\Gamma G(p,q)\varphi(q)\,\mathrm{d}s(q), \qquad (K'\varphi)(p) := \int_\Gamma \frac{\partial G(p,q)}{\partial \mathbf{n}(p)}\varphi(q)\,\mathrm{d}s(q),$$
$$(K\varphi)(p) := \int_\Gamma \frac{\partial G(p,q)}{\partial \mathbf{n}(q)}\varphi(q)\,\mathrm{d}s(q), \qquad (N\varphi)(p) := \text{f.p.} \int_\Gamma \frac{\partial^2 G(p,q)}{\partial \mathbf{n}(p)\partial \mathbf{n}(q)}\varphi(q)\,\mathrm{d}s(q)$$

for $p \in \Gamma$, where $\mathbf{n}(q)$ denotes the outward pointing unit normal to Γ at $q \in \Gamma$. As usual, the initials f.p. in the definition of the hypersingular operator N stand for Hadamard finite-part integral.

The combined field approach consists of looking for a scattered field $u^s = u^s_D$ (resp., $u^s = u^s_N$) in the form

$$u^s(\boldsymbol{r}) = (\mathcal{D}\varphi)(\boldsymbol{r}) - \mathrm{i}\eta(\mathcal{S}\varphi)(\boldsymbol{r}), \quad \boldsymbol{r} \in \mathbb{R}^3 \setminus \Gamma, \tag{2.5}$$

where $\varphi = \varphi_D : \Gamma \to \mathbb{C}$ (resp., $\varphi = \varphi_N : \Gamma \to \mathbb{C}$) is an unknown density function and $\eta \in \mathbb{R}$ is the coupling parameter. The enforcement of Dirichlet and Neumann boundary conditions on Γ leads to the following combined field BIEs:

$$\text{(BW)} \quad \frac{1}{2}\varphi_D(p) + (K\varphi_D)(p) - \mathrm{i}\eta(S\varphi_D)(p) = -u^{\mathrm{inc}}(p), \quad p \in \Gamma, \tag{2.6}$$

and, respectively,

$$\text{(BM)} \quad \frac{\mathrm{i}\eta}{2}\varphi_N(p) - \mathrm{i}\eta(K'\varphi_N)(p) + (N\varphi_N)(p) = -\frac{\partial u^{\mathrm{inc}}(p)}{\partial \mathbf{n}(p)}, \quad p \in \Gamma. \tag{2.7}$$

Both BIEs (2.6) and (2.7) are well-posed in appropriate functional spaces provided that $\eta \in \mathbb{R}$, $\eta \neq 0$ [9].

As is well known, one of the main challenges in the numerical discretization of BIEs (2.6) and (2.7) is posed by the singular character of the kernels of the boundary integral operators defined in equations (2.4) as the integration point q approaches the target point p. Indeed, for a sufficiently regular surface $\Gamma \subset \mathbb{R}^3$ the operators S, K, and K' feature kernels with weak (integrable) singularities of type $\mathcal{O}(|p-q|^{-1})$, while the operators N feature hypersingular kernels of type $\mathcal{O}(|p-q|^{-3})$ as $\Gamma \ni q \to p \in \Gamma$. The numerical evaluation of the layer potentials (2.3), on the other hand, faces the significant challenge of dealing with the nearly singular character of the integral kernels at points $\boldsymbol{r} \in \mathbb{R}^3 \setminus \Gamma$ lying near the boundary at which, although smooth, the integrands exhibit large derivatives that ultimately hinder the accuracy of standard integration procedures.

In what follows, we present a density interpolation method aimed at expressing the boundary integral operators (2.4) and layer potentials (2.3) in terms of surface integrands of prescribed regularity. For presentation simplicity and without loss of

generality, instead of treating each one of the integral operators (2.4) and layer potentials (2.3) separately, we focus on the combined field integral operators of the BW (2.6) and BM (2.7) integral equations and the associated combined field potential (2.5).

3. Kernel regularization via density interpolation. Before we briefly embark on the presentation of the proposed density interpolation method, we first state some useful results of the differential geometry of surfaces that will provide the theoretical basis and the notation for the derivations presented below in this section. The main result of the next section is summarized in Remark 3.1.

3.1. Taylor series on smooth surfaces. We assume throughout this section that Γ is a regular surface. First, given a system of coordinates around $p \in \Gamma$ with $\mathbf{x}(x_1, x_2) = p$, $\mathbf{x} : V \subset \mathbb{R}^2 \to \Gamma$, we define the covariant basis of the tangent space $T_p\Gamma$ of Γ at a point p as

$$\mathbf{e}_i(p) := \frac{\partial \mathbf{x}}{\partial x_i}(p), \quad i = 1, 2.$$

We will follow the usual convention of not using the argument p whenever there is no possibility of confusion. Using the Riemannian metric tensor

$$g_{ij} := \langle \mathbf{e}_i, \mathbf{e}_j \rangle_p = \mathbf{e}_i \cdot \mathbf{e}_j, \quad 1 \leq i, j \leq 2, \tag{3.1}$$

we define the contravariant basis as $\mathbf{e}^i := \sum_{j=1}^2 g^{ij}\mathbf{e}_j$, $i = 1, 2$, in terms of the inverse of the metric tensor $(g^{ij}) = (g_{ij})^{-1}$. We also denote by g the determinant of the metric tensor (g_{ij}), that is, $g = g_{11}g_{22} - g_{12}^2$. With these notations in place, we have that the unit normal at $p \in \Gamma$ is given by $\mathbf{n} = \mathbf{e}_1 \wedge \mathbf{e}_2/\sqrt{g}$.

Given a function $\varphi : \Gamma \to \mathbb{C}$, we define its tangential gradient (or contravariant gradient) by the formula $\langle d\varphi, X \rangle_p = \text{grad } \varphi \cdot X$, for all $X \in T_p\Gamma$, where $d\varphi = \partial_1\varphi\ \mathbf{e}_1 + \partial_2\varphi\ \mathbf{e}_2$ is a 1-form. An explicit formula for grad φ is given by

$$\text{grad } \varphi = (g^{11}\partial_1\varphi + g^{21}\partial_2\varphi)\mathbf{e}_1 + (g^{12}\partial_1\varphi + g^{22}\partial_2\varphi)\mathbf{e}_2 = \partial_1\varphi\ \mathbf{e}^1 + \partial_2\varphi\ \mathbf{e}^2. \tag{3.2}$$

We also define the Hessian of φ, Hess(φ), at $p \in \Gamma$ as the linear operator

$$\text{Hess}(\varphi) : T_p\Gamma \to T_p\Gamma, \quad \text{Hess}(\varphi)(Y) = \nabla_Y \text{grad } \varphi,\ Y \in T_p\Gamma,$$

where ∇ is the Riemannian connection on Γ. The latter can be expressed as

$$\nabla_{\mathbf{e}_i}\mathbf{e}_j = \sum_{\ell=1}^{2} \Gamma_{ij}^{\ell}\mathbf{e}_\ell$$

in terms of the Christoffel symbols defined by $\Gamma_{ij}^{\ell} := \dfrac{\partial \mathbf{e}_i}{\partial x_j} \cdot \mathbf{e}^\ell$.

It can be shown that Hess(φ) can be also viewed as a symmetric bilinear form on $T_p\Gamma$ given by $\text{Hess}(\varphi)(X, Y) = \langle \text{Hess}(\varphi)X, Y \rangle_p$, $X, Y \in T_p\Gamma$. The expression of Hess(φ) can be computed explicitly in the form

$$\text{Hess}(\varphi) = \sum_{i,j=1}^{2} \left(\partial_i\partial_j\varphi - \sum_{\ell=1}^{2} \Gamma_{ij}^{\ell}\partial_\ell\varphi \right) \mathbf{e}^i \otimes \mathbf{e}^j, \tag{3.3}$$

where $\mathbf{e}^i \otimes \mathbf{e}^j = \mathbf{e}^i\ (\mathbf{e}^j)^\top$. For a scalar function $\varphi : \Gamma \to \mathbb{C}$ and a multi-index $\alpha = (\alpha_1, \alpha_2)$, $\alpha_j \in \mathbb{Z}$, $\alpha_j \geq 0$, $j = 1, 2$, we denote

$$\partial^\alpha\varphi := \partial_1^{\alpha_1}\partial_2^{\alpha_2}\varphi = \frac{\partial^{|\alpha|}\varphi}{\partial {x_1}^{\alpha_1}\partial {x_2}^{\alpha_2}}, \tag{3.4}$$

where $|\alpha| = \alpha_1 + \alpha_2$.

Finally, we need to make use of the *exponential map* on Γ. This map is defined on an open neighborhood $\mathcal{U}$ of the origin in $T_p\Gamma$, that is, $\exp_p : \mathcal{U} \subset T_p\Gamma \to \Gamma$, such that, for $v \in \mathcal{U}$ with $|v|$ small enough, $\exp_p(v)$ is defined as the point on Γ which is distance $|v|$ away on the geodesic originating at p and having velocity $v/|v|$ at p. With these notations in place, we are in the position to state *Taylor's formula* in the form

(3.5)
$$\varphi(\exp_p(v)) = \varphi(p) + v^\top \text{grad } \varphi(p) + \frac{1}{2} v^\top \text{Hess}(\varphi)(p)\ v + \mathcal{O}(|v|^3),\ p \in \Gamma,\ v \in T_p(\Gamma),$$

as $|v| \to 0$, or equivalently as

$$\varphi(q) = \varphi(p) + v^\top \text{grad } \varphi(p) + \frac{1}{2} v^\top \text{Hess}(\varphi)(p)\ v + \mathcal{O}(|p-q|^3),\ p, q \in \Gamma, \tag{3.6}$$

as $|p - q| \to 0$, where $v = \exp_p^{-1}(q) \in T_p\Gamma$ in the case when φ is a smooth function defined on Γ. Taylor's formula can be carried to higher-order terms in the form

$$\varphi(q) = \varphi(p) + \sum_{j=1}^{M} \nabla_\Gamma^j \varphi(p)[v \otimes \cdots \otimes v] + \mathcal{O}(|p-q|^{M+1}),\ q, p \in \Gamma, \tag{3.7}$$

as $|p - q| \to 0$, where $v = \exp_p^{-1}(q) \in T_p\Gamma$ and where the jth tensor $(\nabla_\Gamma^j)\varphi : \underbrace{T_p\Gamma \times \cdots \times T_p\Gamma}_{j \text{ times}} \to \mathbb{R}$ is defined recursively as

$$\nabla_\Gamma^j \varphi(Y) = \nabla_Y(\nabla_\Gamma^{j-1}\varphi), \quad j \geq 2, \quad \nabla_\Gamma \varphi := \text{grad } \varphi, \quad Y \in T_p\Gamma,$$

in terms of the Riemannian connection ∇ on Γ. Clearly, as the surface gradient (3.2) and the Hessian (3.3), the higher-order terms $\nabla_\Gamma^j \varphi$, $j \geq 2$, can be expressed as a linear combination of tensor products of the form $\mathbf{e}^{i_1} \otimes \cdots \otimes \mathbf{e}^{i_j}$, $i_\ell \in \{1, 2\}$, whose coefficients, in turn, can be expressed as a linear combination of $\partial^\alpha \varphi$ for all $|\alpha| \leq j$.

Remark 3.1. The main takeaway message of this section is that Taylor's formula (3.7) implies that if two smooth density functions, say φ and ψ, are such that $\partial^\alpha \varphi(p) = \partial^\alpha \psi(p)$ for some $p \in \Gamma$ and for all $|\alpha| \leq M$, where the derivatives are taken with respect to any local parametrization of the surface around the point p, then $\varphi(p) = \psi(q) + \mathcal{O}(|p-q|^{M+1})$ as $\Gamma \ni q \to p \in \Gamma$. In the next section, we will use that result to produce a suitable Taylor-like interpolation of the density that will be used to regularize the boundary integrals.

3.2. Kernel-regularized boundary integral operators and layer potentials. Our density interpolation method relies on the use of certain families of smooth functions $\Phi : \mathbb{R}^3 \times \Gamma \to \mathbb{C}$ that are solutions of the Helmholtz equation

$$\Delta_{\boldsymbol{r}} \Phi(\boldsymbol{r}, p) + k^2 \Phi(\boldsymbol{r}, p) = 0, \quad \boldsymbol{r} \in \mathbb{R}^3 \quad \text{for all } p \in \Gamma.$$

Letting

$$\Phi(q, p) := \lim_{\varepsilon \to 0} \Phi(q + \varepsilon \mathbf{n}(q), p) \quad \text{and} \quad \Phi_n(q, p) := \lim_{\varepsilon \to 0} \nabla \Phi(q + \varepsilon \mathbf{n}(q), p) \cdot \mathbf{n}(q) \tag{3.8}$$

for any given $p \in \Gamma$, and denoting the Dirichlet and Neumann traces of such functions, respectively, we have that an application of the Green's third identity [9, 28] leads to

$$\mathbf{1}_\Omega(\boldsymbol{r})\Phi(\boldsymbol{r}, p) = -\int_\Gamma \frac{\partial G(\boldsymbol{r}, q)}{\partial \mathbf{n}(q)} \Phi(q, p)\, \mathrm{d}s(q) + \int_\Gamma G(\boldsymbol{r}, q)\Phi_n(q, p)\, \mathrm{d}s(q) \tag{3.9}$$

for all $\boldsymbol{r} \in \mathbb{R}^3 \setminus \Gamma$ and $p \in \Gamma$, where $\mathbf{1}_\Omega$ denotes the characteristic function of the domain Ω, i.e., $\mathbf{1}_\Omega = 1$ in Ω and $\mathbf{1}_\Omega = 0$ in $\mathbb{R}^3 \setminus \overline{\Omega}$. Therefore, combining the layer potential (2.5) with formula (3.9) we obtain the following equivalent expression for the combined field potential (2.5):

$$
\begin{aligned}
u^s(\boldsymbol{r}) = -\mathbf{1}_\Omega(\boldsymbol{r})\Phi(\boldsymbol{r},p) + \int_\Gamma \frac{\partial G(\boldsymbol{r},q)}{\partial \mathbf{n}(q)} \left\{\varphi(q) - \Phi(q,p)\right\} \mathrm{d}s(q) \\
- \int_\Gamma G(\boldsymbol{r},q) \left\{\mathrm{i}\eta\varphi(q) - \Phi_n(q,p)\right\} \mathrm{d}s(q),
\end{aligned} \tag{3.10}
$$

which is valid for all $\boldsymbol{r} \in \mathbb{R}^3 \setminus \Gamma$ and $p \in \Gamma$.

Then, letting $\boldsymbol{r} = p + \varepsilon \mathbf{n}(p)$, $\varepsilon > 0$, and taking the limit of both sides of (3.10) as $\varepsilon \to 0^+$, we obtain the following reformulation of the BW integral equation (2.6):

$$
\begin{aligned}
\frac{1}{2}\left\{\varphi(p) - \Phi(p,p)\right\} + \int_\Gamma \frac{\partial G(p,q)}{\partial \mathbf{n}(q)} \left\{\varphi(q) - \Phi(q,p)\right\} \mathrm{d}s(q) \\
- \int_\Gamma G(p,q) \left\{\mathrm{i}\eta\varphi(q) - \Phi_n(q,p)\right\} \mathrm{d}s(q) \; = -u^{\mathrm{inc}}(p) \quad \text{for all } p \in \Gamma,
\end{aligned} \tag{3.11}
$$

where we have utilized the standard jump conditions of the single- and double-layer operators [9, 28].

The scope of the proposed density interpolation technique is to explicitly and efficiently construct a family of functions $\Phi(\boldsymbol{r},p)$ such that the integrands that enter (3.11) are regular (at least bounded) as $\Gamma \ni q \to p \in \Gamma$. To this end, for a given $\eta \in \mathbb{R}$, $\eta \neq 0$, and a scalar function $\varphi : \Gamma \to \mathbb{C}$ which is assumed to be $(M+1)$-times continuously differentiable at $p \in \Gamma$, we say that a family of functions $\Phi(\boldsymbol{r},p)$ defined above satisfies *Taylor-like interpolation conditions of order* $M \geq 0$ at $p \in \Gamma$ if its Dirichlet and Neumann traces, defined in equations (3.8), satisfy

$$
\lim_{q \to p} \partial^\alpha \left\{\varphi(q) - \Phi(q,p)\right\} = 0 \quad \text{for all} \quad |\alpha| \leq M, \tag{3.12a}
$$

$$
\lim_{q \to p} \partial^\alpha \left\{\mathrm{i}\eta\varphi(q) - \Phi_n(q,p)\right\} = 0 \quad \text{for all} \quad |\alpha| \leq M, \tag{3.12b}
$$

respectively, where all the derivatives are taken with respect to q on the surface. In light of the Taylor's formula (3.7), it is clear that

$$
|\varphi(q) - \Phi(q,p)| \lesssim |q-p|^{M+1} \quad \text{and} \quad |\mathrm{i}\eta\varphi(q) - \Phi_n(q,p)| \lesssim |q-p|^{M+1} \tag{3.13}
$$

hold for all $p \in \Gamma$ at which the Taylor-like interpolation conditions (3.12) are satisfied, regardless of the surface parametrization underlaying (3.12) (see Remark 3.1). These estimates imply, in turn, that

$$
\left| \frac{\partial G(p,q)}{\partial \mathbf{n}(q)} \left\{\varphi(q) - \Phi(q,p)\right\} \right| \lesssim |q-p|^M \text{ and } \left| G(p,q) \left\{\mathrm{i}\eta\varphi(q) - \Phi_n(q,p)\right\} \right| \lesssim |q-p|^M.
$$

Therefore, from the estimates above we conclude that the proposed procedure effectively regularizes the singularities of the kernels of the boundary integral operators in (3.11) provided that Φ satisfies the Taylor-like interpolation conditions (3.12) for $M \geq 0$.

Similarly, taking the exterior normal derivative of the expression (3.10) we obtain that the BM integral equation (2.7) can be equivalently expressed as

$$
\begin{aligned}
\frac{1}{2}\left\{\mathrm{i}\eta\varphi(p) - \Phi_n(p,p)\right\} + \int_\Gamma \frac{\partial^2 G(p,q)}{\partial \mathbf{n}(p) \partial \mathbf{n}(q)} \left\{\varphi(q) - \Phi(q,p)\right\} \mathrm{d}s(q) \\
- \int_\Gamma \frac{\partial G(p,q)}{\partial \mathbf{n}(p)} \left\{\mathrm{i}\eta\varphi(q) - \Phi_n(q,p)\right\} \mathrm{d}s(q) = -\frac{\partial u^{\mathrm{inc}}(p)}{\partial \mathbf{n}(p)} \quad \text{for all } p \in \Gamma,
\end{aligned} \tag{3.14}
$$

where the integrands satisfy

$$\left|\frac{\partial^2 G(p,q)}{\partial \mathbf{n}(p)\partial \mathbf{n}(q)}\{\varphi(q)-\Phi(q,p)\}\right| \lesssim |q-p|^{M-2},$$
$$\left|\frac{\partial G(p,q)}{\partial \mathbf{n}(p)}\{\mathrm{i}\eta\varphi(q)-\Phi_n(q,p)\}\right| \lesssim |q-p|^{M}$$

and are at least bounded provided that Φ satisfies the Taylor-like interpolation conditions (3.12) at $p \in \Gamma$ for $M \geq 2$.

Finally, we apply the proposed density interpolation technique to the combined field potential (2.5) at observation points $\boldsymbol{r} \in \mathbb{R}^3 \setminus \Gamma$ near the boundary Γ. Letting $p = p^* = \arg\min_{q\in\Gamma} |\boldsymbol{r}-q| \in \Gamma$ in the formula (3.10) for the combined field potential, we obtain that the corresponding integrands in (3.10) satisfy

$$\left|\frac{\partial G(\boldsymbol{r},q)}{\partial \mathbf{n}(q)}\{\varphi(q)-\Phi(q,p^*)\}\right| \lesssim \frac{|q-p^*|^{M+1}}{|q-\boldsymbol{r}|^2} \leq |q-p^*|^{M-1},$$

$$|G(\boldsymbol{r},q)\{\mathrm{i}\eta\varphi(q)-\Phi_n(q,p^*)\}| \lesssim \frac{|q-p^*|^{M+1}}{|q-\boldsymbol{r}|} \leq |q-p^*|^{M}$$

provided that $\Phi : \mathbb{R}^3\times\Gamma \to \mathbb{C}$ interpolates φ—in the sense of the conditions in (3.12)—at a nearly singular point $p = p^* \in \Gamma$. Clearly, for sufficiently large interpolation orders M, not only do the integrands vanish at p^*, but so do their derivatives. Finally, we mention that kernel-regularized expressions for the gradient of the combined field potential can be obtained by direct differentiation of (3.10).

As we will see in the next section (and in numerical results presented section 6), expressions for the potential and its normal derivative stemming from (3.10), with $p = p^* = \arg\min_{q\in\Gamma} |\boldsymbol{r}-q|$, can be exploited to produce kernel-regularized operators for problems involving multiple obstacles that are close or even intersecting each other.

Remark 3.2. Derivations similar to the ones presented above can be carried out to produce kernel-regularized expressions for all four integral operators of Calderón calculus (2.4). In fact, such expressions for the double-layer and hypersingular operators are given by the left-hand sides of (3.11) and (3.14), respectively, that result from setting $\eta = 0$, where Φ must satisfy (3.12) with the corresponding $\eta = 0$ value. Similarly, kernel-regularized expressions for the single-layer and adjoint double-layer operators are given by the left-hand sides of (3.11) and (3.14), respectively, that result from dividing them by $-\mathrm{i}\eta$ and taking the limit $\eta \to \infty$, where Φ must satisfy (3.12) with the corresponding $(-\mathrm{i}\eta)^{-1} = 0$ value.

Remark 3.3. Maue's formula [9, Theorem 2.23] provides an alternative expression for the hypersingular operator. In fact, for a sufficiently regular surface Γ and density function φ, the hypersingular operator can be equivalently expressed as

$$\begin{aligned}(N\varphi)(p) = {} & k^2 \int_\Gamma G(p,q)(\mathbf{n}(p)\cdot\mathbf{n}(q))\varphi(q)\,\mathrm{d}s(q) \\ & + \text{ p.v.} \int_\Gamma \overrightarrow{\operatorname{curl}}_\Gamma^p G(p,q)\cdot\overrightarrow{\operatorname{curl}}_\Gamma^q \varphi(q)\,\mathrm{d}s(q),\end{aligned} \tag{3.15}$$

where the tangential rotational operator at a point $p \in \Gamma$ is defined as $\overrightarrow{\operatorname{curl}}_\Gamma^p = -\mathbf{n}(p)\wedge \operatorname{grad}_\Gamma^p$ in terms of the surface gradient (3.2) at $p \in \Gamma$ which is here denoted as $\operatorname{grad}_\Gamma^p$. As usual, the initials p.v. in front of the integral sign stand for principal

value integral. Using Maue's formula (3.15), we hence obtain that the BM integral equation (2.7) can be alternatively expressed as

$$\frac{1}{2}\left\{\mathrm{i}\eta\varphi(q)-\Phi_n(q,p)\right\}+k^2\int_\Gamma G(p,q)\mathbf{n}(p)\cdot\mathbf{n}(q)\left\{\varphi(q)-\Phi(q,p)\right\}\,\mathrm{d}s(q)$$
$$+\int_\Gamma \overrightarrow{\mathrm{curl}}^p_\Gamma G(p,q)\cdot\overrightarrow{\mathrm{curl}}^q_\Gamma\left\{\varphi(q)-\Phi(q,p)\right\}\,\mathrm{d}s(q)-\int_\Gamma\frac{\partial G(p,q)}{\partial\mathbf{n}(p)}\left\{\mathrm{i}\eta\varphi(q)-\Phi_n(q,p)\right\}\,\mathrm{d}s(q)$$
$$=-\frac{\partial u^{\mathrm{inc}}(p)}{\partial\mathbf{n}(p)}\quad\text{for all } p\in\Gamma, \tag{3.16}$$

where the most singular integrand satisfies

$$\left|\overrightarrow{\mathrm{curl}}^p_\Gamma G(p,q)\cdot\overrightarrow{\mathrm{curl}}^q_\Gamma\{\varphi(q)-\Phi(q,p)\}\right|\lesssim|q-p|^{M-2}$$

and is at least bounded provided that $M\geq 2$. Both the (3.14) and the (3.16) forms of the BM integral equation are considered in the numerical examples presented in section 6 below.

Remark 3.4. Yet another expression for the hypersingular operator can be easily derived from (3.15) by "moving" the operator $\overrightarrow{\mathrm{curl}}^p_\Gamma$ outside the surface integral, i.e.,

$$\text{p.v.}\int_\Gamma \overrightarrow{\mathrm{curl}}^p_\Gamma G(p,q)\cdot\overrightarrow{\mathrm{curl}}^q_\Gamma\varphi(q)\,\mathrm{d}s(q)=-\,\mathrm{curl}^p_\Gamma\int_\Gamma G(p,q)\overrightarrow{\mathrm{curl}}^q_\Gamma\varphi(q)\,\mathrm{d}s(q), \tag{3.17}$$

where the scalar rotational operator on the right-hand side is defined as $\mathrm{curl}^p_\Gamma=-\mathrm{div}^p_\Gamma\mathbf{n}(p)\wedge$, with div^p_Γ denoting the surface divergence operator at $p\in\Gamma$. It thus follows from (3.17) that the hypersingular operator can be evaluated by applying the proposed technique to the single-layer operator alone, although separate Taylor-like interpolants for each one of the three components of $\overrightarrow{\mathrm{curl}}^q_\Gamma\varphi(q)$ and $\mathbf{n}(q)\varphi(q)$ are needed. This approach is utilized in section 6 to produce accurate BEM discretizations of the BM integral equation using $M=0$ and $M=1$.

3.3. Multiple-scattering approach to scattering by composite surfaces. Let Ω_j, $j=1,2$, be open and simply connected domains with smooth boundaries $\Gamma_j=\partial\Omega_j$. Suppose $\Omega\subset\mathbb{R}^3$ is given by the union $\Omega=\Omega_1\cup\Omega_2$, where $\Omega_1\cap\Omega_2\neq\emptyset$. For the sake of conciseness and simplicity, we focus here on the exterior Dirichlet problem (2.1) which we proceed to formulate as a multiple scattering problem encompassing the two obstacles Ω_1 and Ω_2. This formulation is advantageous in many practical applications where suitable discrete representations of the "combined surface" $\Gamma=\partial(\Omega_1\cup\Omega_2)$ (in terms of surface meshes in the case of BEMs or manifold representations in terms of coordinate patches in the case of Nyström methods) are difficult to produce, but separate discretizations of its component parts, $\Gamma_1=\partial\Omega_1$ and $\Gamma_2=\partial\Omega_2$, are easy to generate. An important example in this regard are van der Waals molecular surfaces, which are given by the union of a typically large number of spherical atoms (see, e.g., [8]).

Instead of considering the BW integral equation (2.6) on $\Gamma=\partial(\Omega_1\cup\Omega_2)$, we pose it on $\tilde\Gamma=\Gamma_1\cup\Gamma_2$. Letting $\tilde\varphi:\tilde\Gamma\to\mathbb{C}$ be a density function, we look for the scattered field in the form of the combined field potential $u^s(\boldsymbol{r})=(\tilde{\mathcal{D}}\tilde\varphi)(\boldsymbol{r})-\mathrm{i}\eta(\tilde{\mathcal{S}}\tilde\varphi)(\boldsymbol{r})$, where $\tilde{\mathcal{D}}$ and $\tilde{\mathcal{S}}$ are the double- and single-layer potentials in (2.3) but defined in terms of surface integrals over $\tilde\Gamma$. The enforcement of the Dirichlet boundary condition on $\tilde\Gamma$ yields the integral equation

$$\frac{1}{2}\begin{pmatrix}\varphi_1\\ \varphi_2\end{pmatrix}+\begin{pmatrix}K_{11}-\mathrm{i}\eta S_{11} & K_{12}-\mathrm{i}\eta S_{12}\\ K_{21}-\mathrm{i}\eta S_{21} & K_{22}-\mathrm{i}\eta S_{22}\end{pmatrix}\begin{pmatrix}\varphi_1\\ \varphi_2\end{pmatrix}=\begin{pmatrix}f_1\\ f_2\end{pmatrix} \tag{3.18}$$

on $\tilde{\Gamma}$ for the unknown density function $\tilde{\varphi}$, where $\varphi_j = \tilde{\varphi}|_{\Gamma_j}$ and $f_j|_{\Gamma_j} = -u^{\rm inc}|_{\Gamma_j}$, $j = 1, 2$. The operators S_{ij} and K_{ij}, $i, j = 1, 2$, in (3.18) are the single- and double-layer operators in (2.4) but defined in terms of boundary integrals over Γ_i and target points $p \in \Gamma_j$. Note that the Dirichlet data (f_1, f_2) in (3.18) requires the incident field $u^{\rm inc}$ to be defined on $\tilde{\Gamma} \setminus \Gamma$. Typically, $u^{\rm inc}$ is given by an explicit expression that can be directly evaluated almost everywhere in $\mathbb{R}^3$ including $\tilde{\Gamma}$. If that is not the case, (f_1, f_2) can be defined by simply extending $u^{\rm inc}$ to $\tilde{\Gamma} \setminus \Gamma$ by zero.

In order to evaluate the integral operators in (3.18), we apply the proposed technique to each one of the operators involving integration over the closed surfaces Γ_1 and Γ_2. This is achieved by regularizing $I/2 + K_{ij} - \mathrm{i}\eta S_{ij}$ for $i = j$ as an integral operator acting on Γ_i using (3.11), and regularizing $K_{i,j} - \mathrm{i}\,\eta S_{ij}$ for $i \neq j$ as a layer potential that involves integration over Γ_i and evaluation at target points $\boldsymbol{r} \in \Gamma_j$ using (3.10).

The effectiveness of this approach is demonstrated by numerical examples based on the BEM presented in section 6. A more extensive study of the multiple-scattering approach to scattering by composite surface—that, in particular, will include the BM integral equation (2.7)—will be presented in a future contribution.

In the next section, we present an explicit construction of families of functions Φ such that the conditions (3.12) are satisfied for any given smooth function φ.

4. Interpolating functions. This section is devoted to the construction of the functions Φ introduced in the previous section. Specifically, we look for expressions of the kind

$$\Phi(\boldsymbol{r}, p) := \sum_{|\alpha|=0}^{M} \partial^\alpha \varphi(p) \Phi_\alpha^{(1)}(\boldsymbol{r}, p) + \mathrm{i}\eta \sum_{|\alpha|=0}^{M} \partial^\alpha \varphi(p) \Phi_\alpha^{(2)}(\boldsymbol{r}, p), \tag{4.1}$$

where the derivatives $\partial^\alpha \varphi$ are defined as in (3.4) and where the expansion functions $\Phi_\alpha^{(1)}$ and $\Phi_\alpha^{(2)}$ are taken to be linear combinations of planewaves:

$$\Phi_\alpha^{(1)}(\boldsymbol{r}, p) := \sum_{\ell=1}^{L} a_{\ell,\alpha}(p) W_\ell(\boldsymbol{r} - p) \quad \text{and} \quad \Phi_\alpha^{(2)}(\boldsymbol{r}, p) := \sum_{\ell=1}^{L} b_{\ell,\alpha}(p) W_\ell(\boldsymbol{r} - p), \tag{4.2}$$

where $W_\ell(\boldsymbol{r} - p) = \exp\{\mathrm{i}k\boldsymbol{d}_\ell \cdot (\boldsymbol{r} - p)\}$, $\ell = 1, \ldots, L$, have distinct directions $\boldsymbol{d}_\ell$ ($|\boldsymbol{d}_\ell| = 1$). The directions $\boldsymbol{d}_\ell$ may depend on $p \in \Gamma$, in which case we make the dependence explicit in the notation $\boldsymbol{d}_\ell = \mathbf{d}_\ell(p)$. Clearly, any linear combination of the form (4.2) amounts to a homogeneous solution of the Helmholtz equation in the variable $\boldsymbol{r}$.

The following lemma, whose proof follows directly from Taylor's theorem in two dimensions, establishes simple point conditions on the traces of the expansion functions (4.2) that guarantee that the interpolation requirements (3.12) are satisfied.

LEMMA 4.1. *Let $\Phi : \mathbb{R}^3 \times \Gamma \to \mathbb{C}$ be given by* (4.1)*, where $\Phi_\alpha^{(j)} : \mathbb{R}^3 \times \Gamma \to \mathbb{C}$, $|\alpha| \leq M$, $j = 1, 2$, are the linear combinations of planewaves defined in* (4.2)*. Then, sufficient conditions for Φ to satisfy* (3.12) *at $p \in \Gamma$ are that the Dirichlet trace $\Phi_\alpha^{(j)}(q, p)$ and the Neumann trace $\Phi_{n,\alpha}^{(j)}(q, p) = \lim_{\epsilon \to 0} \nabla_{\boldsymbol{r}} \Phi_\alpha^{(j)}(q + \epsilon \mathbf{n}(q), p) \cdot \mathbf{n}(q)$, where $q \in \Gamma$ and $j = 1, 2$, satisfy*

$$\partial^\beta \Phi_\alpha^{(1)}(p, p) = \begin{cases} 1 & \text{if} \quad \beta = \alpha, \\ 0 & \text{if} \quad \beta \neq \alpha, \end{cases} \qquad \partial^\beta \Phi_{n,\alpha}^{(1)}(p, p) = 0, \tag{4.3a}$$

$$\partial^\beta \Phi_\alpha^{(2)}(p, p) = 0 \quad \text{and} \quad \partial^\beta \Phi_{n,\alpha}^{(2)}(p, p) = \begin{cases} 1 & \text{if} \quad \beta = \alpha, \\ 0 & \text{if} \quad \beta \neq \alpha \end{cases} \tag{4.3b}$$

for all subindices $\beta \in \mathbb{Z}_+^2$ such that $|\beta| \leq M$.

The following two sections address the problem of finding explicit expressions for $\Phi_\alpha^{(1)}$ and $\Phi_\alpha^{(2)}$, $|\alpha| \leq M$, by utilizing the point conditions (4.3).

4.1. Closed-form planewave expansion functions in the case $M = 1$. In this section, we find closed-form expressions for the families of functions $\{\Phi_\alpha^{(1)}\}_{|\alpha|\leq M}$ and $\{\Phi_\alpha^{(2)}\}_{|\alpha|\leq M}$, defined in (4.2), whose traces satisfy the requirements in Lemma 4.1 for the interpolation order $M = 1$.

We thus search for functions $\{\Phi_\alpha^{(1)}\}_{|\alpha|\leq 1}$ and $\{\Phi_\alpha^{(2)}\}_{|\alpha|\leq 1}$ that are linear combinations of planewaves whose directions $\boldsymbol{d}_\ell$ depend on $p \in \Gamma$, that is, $W_\ell(\boldsymbol{r} - p) = \exp\{\mathrm{i}k\mathbf{d}_\ell(p) \cdot (\boldsymbol{r} - p)\}$, $\ell = 1, \ldots, L$. The planewave directions $\mathbf{d}_\ell(p)$ are expressed in terms of the basis $\{\boldsymbol{\tau}_1(p), \boldsymbol{\tau}_2(p), \mathbf{n}(p)\}$, that is,

$$\mathbf{d}_\ell(p) = d_{\ell,1}\boldsymbol{\tau}_1(p) + d_{\ell,2}\boldsymbol{\tau}_2(p) + d_{\ell,3}\mathbf{n}(p), \quad |\mathbf{d}_\ell(p)| = 1,$$

where the unitary contravariant vectors $\boldsymbol{\tau}_j(p)$, $j = 1, 2$, are defined by

$$\boldsymbol{\tau}_1 := \sqrt{\frac{g}{g_{22}}}\mathbf{e}^1 \quad \text{and} \quad \boldsymbol{\tau}_2 := \sqrt{\frac{g}{g_{11}}}\mathbf{e}^2 \tag{4.4}$$

in terms of the Riemann metric tensor (g_{ij}) in (3.1) and its determinant g. Note that we dropped the dependence on p of all the quantities in equations (4.4), as there is no risk of confusion.

We begin by defining, for $p \in \Gamma$ and a direction $\mathbf{d}(p)$ (which may not be unitary), the following functions:

$$S(\boldsymbol{r}, p, \mathbf{d}(p)) := \sin\left(k\mathbf{d}(p) \cdot (\boldsymbol{r} - p)\right) \quad \text{and} \quad C(\boldsymbol{r}, p, \mathbf{d}(p)) := \cos\left(k\mathbf{d}(p) \cdot (\boldsymbol{r} - p)\right) \tag{4.5}$$

for $\boldsymbol{r} \in \mathbb{R}^3$. Clearly, for unitary directions $\mathbf{d}_1(p)$ and $\mathbf{d}_2(p)$, the products

$$C\left(\cdot, \cdot, \frac{\mathbf{d}_1(p)}{\sqrt{2}}\right) C\left(\cdot, \cdot, \frac{\mathbf{d}_2(p)}{\sqrt{2}}\right), \quad C\left(\cdot, \cdot, \frac{\mathbf{d}_1(p)}{\sqrt{2}}\right) S\left(\cdot, \cdot, \frac{\mathbf{d}_2(p)}{\sqrt{2}}\right),$$

$$S\left(\cdot, \cdot, \frac{\mathbf{d}_1(p)}{\sqrt{2}}\right) S\left(\cdot, \cdot, \frac{\mathbf{d}_2(p)}{\sqrt{2}}\right)$$

are linear combinations of planewaves of the form (4.2) with (unitary) directions $\frac{1}{\sqrt{2}}(\mathbf{d}_1(p) + \mathbf{d}_2(p))$ and $\frac{1}{\sqrt{2}}(\mathbf{d}_1(p) - \mathbf{d}_2(p))$ provided that $\mathbf{d}_1(p) \cdot \mathbf{d}_2(p) = 0$.

The following lemma introduces the sought linear combinations of planewaves.

LEMMA 4.2. *Let S and C be the functions defined in* (4.5)*, and denote by $L = -\mathbf{e}_1 \cdot \partial_1 \mathbf{n} = \partial_1^2 \mathbf{x} \cdot \mathbf{n}$, $M = -\mathbf{e}_1 \cdot \partial_2 \mathbf{n} = -\mathbf{e}_2 \cdot \partial_1 \mathbf{n} = \partial_1 \partial_2 \mathbf{x} \cdot \mathbf{n}$, and $N = -\mathbf{e}_2 \cdot \partial_2 \mathbf{n} = \partial_2^2 \mathbf{x} \cdot \mathbf{n}$ the second fundamental form coefficients at $p \in \Gamma$. Then, the Dirichlet and Neumann traces of*

$$\Phi_{(0,0)}^{(2)}(\boldsymbol{r}, p) := \frac{1}{k} S\left(\boldsymbol{r}, p, \mathbf{n}(p)\right), \tag{4.6a}$$

$$\Phi_{(1,0)}^{(2)}(\boldsymbol{r}, p) := \frac{2}{k^2}\sqrt{\frac{g_{22}}{g}} S\left(\boldsymbol{r}, p, \frac{\mathbf{n}(p)}{\sqrt{2}}\right) S\left(\boldsymbol{r}, p, \frac{\boldsymbol{\tau}_1(p)}{\sqrt{2}}\right), \tag{4.6b}$$

$$\Phi_{(0,1)}^{(2)}(\boldsymbol{r}, p) := \frac{2}{k^2}\sqrt{\frac{g_{11}}{g}} S\left(\boldsymbol{r}, p, \frac{\mathbf{n}(p)}{\sqrt{2}}\right) S\left(\boldsymbol{r}, p, \frac{\boldsymbol{\tau}_2(p)}{\sqrt{2}}\right) \tag{4.6c}$$

and

$$\Phi^{(1)}_{(0,0)}(\boldsymbol{r},p) := C\left(\boldsymbol{r},p,\mathbf{n}(p)\right), \tag{4.7a}$$

$$\Phi^{(1)}_{(1,0)}(\boldsymbol{r},p) := \frac{1}{k}\sqrt{\frac{g_{22}}{g}}S\left(\boldsymbol{r},p,\boldsymbol{\tau}_1(p)\right) - \left\{\frac{g_{12}M - g_{22}L}{g}\right\}\Phi^{(2)}_{(1,0)}(\boldsymbol{r},p) - \left\{\frac{g_{12}N - g_{22}M}{g}\right\}\Phi^{(2)}_{(0,1)}(\boldsymbol{r},p), \tag{4.7b}$$

$$\Phi^{(1)}_{(0,1)}(\boldsymbol{r},p) := \frac{1}{k}\sqrt{\frac{g_{11}}{g}}S\left(\boldsymbol{r},p,\boldsymbol{\tau}_2(p)\right) - \left\{\frac{g_{12}L - g_{11}M}{g}\right\}\Phi^{(2)}_{(1,0)}(\boldsymbol{r},p) - \left\{\frac{g_{12}M - g_{11}N}{g}\right\}\Phi^{(2)}_{(0,1)}(\boldsymbol{r},p) \tag{4.7c}$$

satisfy the requirements (4.3b) *and* (4.3a) *of Lemma* 4.1*, respectively, for* $M = 1$.

Proof. The proof follows directly from the computation of the tangential derivatives of $\Phi^{(1)}_\alpha$ and $\Phi^{(2)}_\alpha$ at $\boldsymbol{r} = p \in \Gamma$ and the use of the identities [13]

$$\begin{aligned}\partial_1\mathbf{n} &= -\left(g^{11}L + g^{12}M\right)\mathbf{e}_1 - \left(g^{21}L + g^{22}M\right)\mathbf{e}_2,\\ \partial_2\mathbf{n} &= -\left(g^{11}M + g^{12}N\right)\mathbf{e}_1 - \left(g^{21}M + g^{22}N\right)\mathbf{e}_2,\end{aligned} \tag{4.8}$$

where (g^{ij}) denotes the inverse of the metric tensor (g_{ij}). ∎

The extension of the trigonometric ansatz technology utilized above to the construction of closed-form families of functions $\{\Phi^{(1)}_\alpha\}_{|\alpha|\le M}$ and $\{\Phi^{(2)}_\alpha\}_{|\alpha|\le M}$ that satisfy conditions in (4.3) for $M \ge 2$ is challenging. In particular, additional distinct planewave directions ought to be incorporated in the ansatz. Because of the aforementioned difficulties, we advocate for the algebraic approach presented in the following section to construct high-order planewave expansion functions in the case $M \ge 2$.

4.2. Higher-order planewave expansion functions. In this section, we develop a purely algebraic algorithm to construct expansion functions $\{\Phi^{(1)}_\alpha\}_{|\alpha|\le M}$ and $\{\Phi^{(2)}_\alpha\}_{|\alpha|\le M}$ at a given (regular) point $p \in \Gamma$. Unlike the analytical approach presented in the previous section, we now select a collection of planewave directions $\{\boldsymbol{d}_\ell\}_{\ell=1}^{\ell=L}$ that are independent of $p \in \Gamma$. While the desired interpolation order M and the number L of planewave directions are parameters in our algorithm, the planewave directions themselves can be selected either randomly or uniformly from the unit sphere in three dimensions.

It is clear from Lemma 4.1 that in order to find the desired expansion coefficients $\{a_{\ell,\alpha}\}_{\ell=1,|\alpha|\le M}^{\ell=L}$ (resp., $\{b_{\ell,\alpha}\}_{\ell=1,|\alpha|\le M}^{\ell=L}$) that determine the expansion functions $\{\Phi^{(1)}_\alpha\}_{|\alpha|\le M}$ (resp., $\{\Phi^{(2)}_\alpha\}_{|\alpha|\le M}$) at $p \in \Gamma$, one has to impose the $N = (M+1)(M+2)$ independent conditions (4.3a) (resp., (4.3b)), which have to be satisfied exactly. Consequently, a solvable linear system for the coefficients could be produced provided that the number of planewave directions satisfies $L \ge N$. In order to form such a linear system, we proceed to sort the $N/2$ indices $\alpha = (\alpha_1, \alpha_2)$ satisfying $\alpha_1 + \alpha_2 \le M$ by introducing a bijective mapping $J : \{|\alpha| \le M\} \to \{1, \ldots, N/2\}$. Therefore, letting $\boldsymbol{\delta}_j$, $j = 1, \ldots, N$, denote the canonical vectors of $\mathbb{R}^N$, we have that conditions (4.3a) lead to the linear system

$$\boldsymbol{C}(p)\mathbf{a}_j(p) = \boldsymbol{\delta}_j, \quad j = 1, \ldots, N/2, \tag{4.9}$$

for the coefficient vector $\mathbf{a}_j = [a_{1,J^{-1}(j)}, \ldots, a_{L,J^{-1}(j)}]^T \in \mathbb{C}^L$, while conditions (4.3b) yield the system

$$\boldsymbol{C}(p)\mathbf{b}_j(p) = \boldsymbol{\delta}_{j+N/2}, \quad j = 1, \ldots, N/2, \tag{4.10}$$

for the coefficient vector $\mathbf{b}_j = [b_{1,J^{-1}(j)}, \ldots, b_{L,J^{-1}(j)}]^T \in \mathbb{C}^L$, where $\boldsymbol{C}(p)$ is an $N \times L$ complex-valued matrix. Note that we have assumed in these derivations that the first $N/2$ rows of $\boldsymbol{C}(p)$ correspond to the conditions on the Dirichlet traces, while the remaining $N/2$ rows correspond to the conditions on the Neumann traces.

In the case when $L > N$, the solution of the linear systems (4.9) and (4.10) must be understood in the least-squares sense. Letting $\boldsymbol{C}^\dagger(p) = \left[\mathbf{c}_1^\dagger(p), \ldots, \mathbf{c}_N^\dagger(p)\right] \in \mathbb{C}^{L\times N}$ denote the Moore–Penrose pseudoinverse of $\boldsymbol{C}(p)$, that is, $\boldsymbol{C}(p)\boldsymbol{C}^\dagger(p) = \boldsymbol{I}$, with $\boldsymbol{I} \in \mathbb{R}^{N\times N}$ being the identity matrix and $\boldsymbol{C}(p)$ being full-rank, the unknown vectors $\mathbf{a}_j$ and $\mathbf{b}_j$, respectively, are given by

$$\mathbf{a}_j(p) = \mathbf{c}_j^\dagger(p) \quad \text{and} \quad \mathbf{b}_j(p) = \mathbf{c}_{j+N/2}^\dagger(p), \quad j = 1, \ldots, N/2. \tag{4.11}$$

Note that under the assumption that $\boldsymbol{C}(p)$ is full-rank, $\boldsymbol{C}^\dagger(p)$ can be computed explicitly via the formula $\boldsymbol{C}^\dagger(p) = \boldsymbol{C}^*(p)\left(\boldsymbol{C}(p)\boldsymbol{C}^*(p)\right)^{-1}$, where $\boldsymbol{C}^*$ denotes the Hermitian transpose of $\boldsymbol{C}$.

We present in the supplementary materials SM1, linked from the main article webpage, a recursive approach to compute the entries of the matrices $\boldsymbol{C}(p)$ in the case $M = 3$.

Remark 4.3. We have found it difficult to prove whether for a given set of distinct planewave directions $\{\boldsymbol{d}_\ell\}_{\ell=1}^{\ell=L}$ the matrix $\boldsymbol{C}(p) \in \mathbb{C}^{(M+1)(M+2)\times L}$ is full-rank for any $p \in \Gamma$. We have observed in numerical experiments, however, that when $L = (M+1)(M+2)$ the resulting square matrix $\boldsymbol{C}(p)$ is very ill conditioned for some points $p \in \Gamma$. We thus recommend in general to select $L > (M+1)(M+2)$ in order to sufficiently enrich the column space of $\boldsymbol{C}(p)$ so that its pseudoinverse $\boldsymbol{C}^\dagger(p)$ becomes computable. In practice, large enough $\mathcal{O}(M^2)$ numbers of planewave directions, selected from a "uniform" spherical grid, give rise to numerically invertible matrices $\boldsymbol{C}(p)\boldsymbol{C}^*(p)$ from where the $\boldsymbol{C}^\dagger(p)$ can be computed. In detail, the planewave directions for the construction of numerical PWDI interpolants used throughout this paper are given by $(\cos\theta_m \sin\phi_n, \sin\theta_m \sin\phi_n, \cos\phi_n)$, where $\theta_m = 2\pi(m-1/2)/L_\theta$ for $m = 1, \ldots, L_\theta$ and $\phi_n = \pi(n-1/2)/L_\phi$ for $n = 1, \ldots, L_\phi$, with $L = L_\theta \times L_\phi = 2\times 2$, 4×3, 5×4, 6×5 for interpolation orders $M = 0, 1, 2, 3$, respectively.

5. Numerical evaluation of integral operators and layer potentials.

This section presents Nyström and Galerkin BEM discretization schemes, based on standard quadrature rules, for the numerical evaluation of the kernel-regularized integral operators and layer potentials associated to the combined field integral equations (2.6) and (2.7).

5.1. Chebyshev-based Nyström method.

We here briefly describe the 3D BIE method introduced in our previous contribution [30]. The surface Γ is represented as the union $\Gamma = \bigcup_{m=1}^{N_p} \overline{\mathcal{P}^m}$ of nonoverlapping patches $\mathcal{P}^m$, $m = 1, \ldots, N_p$, where $\mathcal{P}^m \cap \mathcal{P}^l = \emptyset$ if $m \neq l$. It is assumed (throughout this section) that each surface patch $\mathcal{P}^m$ has associated to it a bijective $\mathcal{C}^\infty$ coordinate map $\mathbf{x}^m : \mathcal{H} \to \overline{\mathcal{P}^m}$,

$$\mathbf{x}^m(\boldsymbol{\xi}) := \left(x_1^m(\xi_1,\xi_2), x_2^m(\xi_1,\xi_2), x_3^m(\xi_1,\xi_2)\right), \quad m = 1, \ldots, N_p \quad (\boldsymbol{\xi} = (\xi_1,\xi_2)), \tag{5.1}$$

where $\mathcal{H} = [-1,1]\times[-1,1] \subset \mathbb{R}^2$. Furthermore, the coordinate maps (5.1) are selected in such a way that the unit normal $\mathbf{n}^m(\boldsymbol{\xi}) = \partial_1\mathbf{x}^m(\boldsymbol{\xi}) \wedge \partial_2\mathbf{x}^m(\boldsymbol{\xi})/|\partial_1\mathbf{x}^m(\boldsymbol{\xi}) \wedge \partial_2\mathbf{x}^m(\boldsymbol{\xi})|$ at the point $\mathbf{x}^m(\boldsymbol{\xi}) \in \mathcal{P}^m$ points outward to the surface Γ. The surface integral of a sufficiently regular function $F : \Gamma \to \mathbb{R}$—such as the integrands in (3.11), (3.14), and (3.10)—can then be expressed as

$$\int_\Gamma F(\boldsymbol{x})\,\mathrm{d}s = \sum_{m=1}^{N_p} \int_{\mathcal{H}} F\left((\mathbf{x}^m(\boldsymbol{\xi}))\right) |\partial_1\mathbf{x}^m(\boldsymbol{\xi}) \wedge \partial_2\mathbf{x}^m(\boldsymbol{\xi})|\,\mathrm{d}\boldsymbol{\xi} = \int_{\mathcal{H}} f(\boldsymbol{\xi})\,\mathrm{d}\boldsymbol{\xi}.$$

In order to numerically evaluate the integral above with high precision, we utilize open Chebyshev grids in the parameter space $\mathcal{H}$. Accordingly, $\mathcal{H}$ is discretized by means of the so-called Fejér's first quadrature rule [12], which yields the approximation

$$\int_{\mathcal{H}} f(\boldsymbol{\xi})\,\mathrm{d}\boldsymbol{\xi} \approx \sum_{i=1}^{N}\sum_{j=1}^{N} f(t_i,t_j)\omega_i\omega_j, \tag{5.2}$$

where the quadrature points t_j are the Chebyshev zero points

$$t_j := \cos(\vartheta_j), \quad \vartheta_j := \frac{(2j-1)\pi}{2N}, \quad j = 1,\dots,N, \tag{5.3}$$

and the Fejér quadrature weights are given by

$$\omega_j := \frac{2}{N}\left(1 - 2\sum_{\ell=1}^{[N/2]} \frac{1}{4\ell^2-1}\cos(2\ell\vartheta_j)\right), \quad j = 1,\dots,N. \tag{5.4}$$

A key feature of this discretization scheme is that the quadrature rule (5.2) yields spectral (superalgebraic) accuracy for integration of smooth $C^\infty(\mathcal{H})$ functions. As expected, however, slower convergence rates are achieved for less regular integrands (such as surface density functions associated to problems of scattering by piecewise smooth obstacles). Yet another important feature of this discretization scheme is that all the partial derivatives of the coordinate maps $\mathbf{x}^m$, unit normals $\mathbf{n}^m$, and functions $\varphi(\mathbf{x}^m(\boldsymbol{\xi}))$ that are needed for the construction of the planewave density interpolant $\Phi : \mathbb{R}^3 \times \Gamma \to \mathbb{C}$ can be efficiently and accurately computed at the grid points (t_i, t_j), $1 \le i,j \le N$, by means of FFT differentiation. More details can be found in [30].

Finally, the proposed procedure for the numerical evaluation of the BW combined field operator $K - \mathrm{i}\eta S$, using the method of section 4.2, is summarized in Algorithm 5.1. A completely analogous procedure can be followed for evaluation of the BM combined field operator $N - \mathrm{i}\eta K'$.

5.2. Galerkin boundary element method. This section concerns the use of the proposed planewave density interpolation method within the standard second-order Galerkin BEM discretization using triangular surface meshes.

To fix ideas, we consider once again the BW boundary integral equation (2.6) which upon constructing an appropriate density interpolation function $\Phi : \mathbb{R}^3\times\Gamma \to \mathbb{C}$ can be equivalently expressed (in strong form) as (3.11). Throughout this section, we assume that $\Omega \subset \mathbb{R}^3$ is a bounded Lipschitz polyhedral domain. Therefore, associated to the surface $\Gamma = \partial\Omega$ there is a triangulation $\mathcal{T}_h$ such that $\Gamma = \overline{\bigcup_{T\in\mathcal{T}_h} T}$. Note that both the single- and the double-layer operators are bounded on $H^{1/2}(\Gamma)$ and that the Green's identities used in the derivation of (3.11) still hold true for Γ being

Algorithm 5.1. Nyström evaluation of the forward map $(K - \mathrm{i}\eta S)\varphi$.

Require: Grids $\{\boldsymbol{x}_{i,j}^k\}_{i,j=1}^{i,j=N} \subset \mathcal{P}^k$, $k = 1, \dots, N_p$, corresponding to the discretization of the surface Γ using N_p nonoverlapping patches, generated using Chebyshev grids in the parameter space $\mathcal{H}$; discrete density function $\varphi(\boldsymbol{x}_{i,j}^k) = \phi_{i,j}^k$, $i, j = 1, \dots, N$. $k = 1, \dots, N_p$; planewave interpolation order M; planewave directions $\boldsymbol{d}_\ell$, $\ell = 1, \dots, L$.

for k from 1 to N_p **do**

Compute $\partial^\alpha \varphi$ of all orders $|\alpha| \leq M$ on the patch $\mathcal{P}^k$ using FFT-based spectral differentiation of the 2D array $\{\phi_{i,j}^k\}_{i,j=1}^{i,j=N}$

end for

Set $I_{i,j}^k = 0$ for $i, j = 1, \dots, N$ and $k = 1, \dots, N_p$

for each grid point $\boldsymbol{x}_{i,j}^k$ **do**

Generate the coefficients $a_{\ell,\alpha_r}(\boldsymbol{x}_{i,j}^k)$ and $b_{\ell,\alpha_r}(\boldsymbol{x}_{i,j}^k)$ for $\ell = 1, \dots, L$ and $r = 1, \dots, (M+1)(M+2)/2$

Compute the interpolating function Φ (4.1) using the derivatives $\partial^\alpha \varphi$ at $\boldsymbol{x}_{i,j}^k$ and the coefficients a_{ℓ,α_r} and b_{ℓ,α_r}

for m from 1 to N_p **do**

Evaluate the approximate integral $I = \sum_{\boldsymbol{x}_{p,q}^m \in \mathcal{P}^m} f(\boldsymbol{x}_{p,q}^m) w_{p,q}^m \approx \int_{\mathcal{P}^m} f(\boldsymbol{y})\,\mathrm{d}s$, with $f(\boldsymbol{y}) = -\frac{\varphi(\boldsymbol{x}_{i,j}^k)}{2} + \frac{\partial G(\boldsymbol{x}_{i,j}^k, \boldsymbol{y})}{\partial n(\boldsymbol{y})}\{\varphi(\boldsymbol{y}) - \Phi(\boldsymbol{y}, \boldsymbol{x}_{i,j}^k)\} - G(\boldsymbol{x}_{i,j}^k, \boldsymbol{y})\left\{\mathrm{i}\eta\varphi(\boldsymbol{y}) - \partial_n \Phi(\boldsymbol{y}, \boldsymbol{x}_{i,j}^k)\right\}$, using Fejér's quadrature rule

Update $I_{i,j}^k = I_{i,j}^k + I$

end for

end for

return $I_{i,j}^k$ for $i, j = 1, \dots N$ and $k = 1, \dots, N_p$.

Lipschitz [27]. Therefore, assuming that $u^{\mathrm{inc}}|_\Gamma \in H^{1/2}(\Gamma)$, we readily have that the variational formulation of (3.11)—or, equivalently, (2.6)—reads as follows: Find $\varphi \in H^{1/2}(\Gamma)$ such that

(5.5)
$$\int_\Gamma \left\{ \frac{1}{2}\{\varphi(p) - \Phi(p,p)\} + \int_\Gamma \frac{\partial G(p,q)}{\partial \mathbf{n}(q)}\{\varphi(q) - \Phi(q,p)\}\,\mathrm{d}s(q) \right\} \psi(p)\,\mathrm{d}s(p)$$
$$- \int_\Gamma \left\{ \int_\Gamma G(p,q)\{\mathrm{i}\eta\varphi(q) - \Phi_n(q,p)\}\,\mathrm{d}s(q) \right\} \psi(p)\,\mathrm{d}s(p) = -\int_\Gamma u^{\mathrm{inc}}(p)\psi(p)\,\mathrm{d}s(p)$$

for all test functions $\psi \in H^{-1/2}(\Gamma)$.[2] In order to find an approximate weak solution $\varphi_h \in H^{1/2}(\Gamma)$ of (5.5), we resort to a Galerkin BEM for which we consider the (finite-dimensional) subspace $W_h = \{v \in C(\Gamma) : v|_T \text{ is a linear function } \forall T \in \mathcal{T}_h\} \subset H^{1/2}(\Gamma) \subset H^{-1/2}(\Gamma)$. Clearly, the set $\{v_j\}_{j=1}^N$ of linear polynomials supported on $\bigcup_{p_j \in T} T$ satisfying the condition $v_j(p_i) = \delta_{i,j}$ for all $i, j = 1 \dots, N$, where p_j, $j = 1, \dots, N$ are the mesh nodes, forms a basis of the subspace W_h. In detail, letting p_{τ_1}, p_{τ_2}, and p_{τ_3}, with $\tau_1, \tau_2, \tau_3 \in \{1, \dots, N\}$, denote the vertices of a triangle $T \in \mathcal{T}_h$,

[2] We assume here the continuous extension of the standard real pairing $(u, v) = \int_\Gamma uv\,\mathrm{d}s$ for $u, v \in L^2(\Gamma)$ to the dual pairing $\langle \cdot, \cdot \rangle_{H^{1/2}(\Gamma) \times H^{-1/2}(\Gamma)}$.

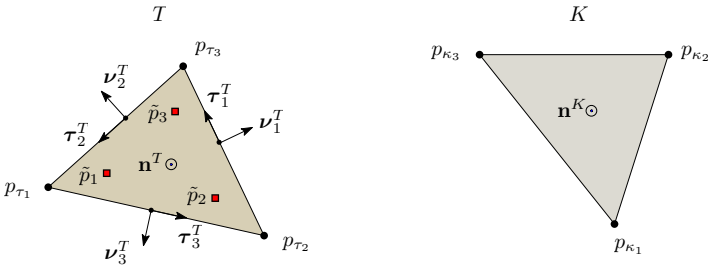

FIG. 1. *Notation used for the the mesh triangles in the outer (T) and inner (K) integrals in* (5.12) *and in the Algorithm* 5.2.

and defining the unit vectors (see Figure 1)

$$\boldsymbol{\tau}_1^T = \frac{p_{\tau_3} - p_{\tau_2}}{|p_{\tau_3} - p_{\tau_2}|}, \qquad \boldsymbol{\tau}_2^T = \frac{p_{\tau_1} - p_{\tau_3}}{|p_{\tau_1} - p_{\tau_3}|}, \qquad \boldsymbol{\tau}_3^T = \frac{p_{\tau_2} - p_{\tau_1}}{|p_{\tau_2} - p_{\tau_1}|},$$

$$\boldsymbol{\nu}_1^T = \boldsymbol{\tau}_1^T \wedge \mathbf{n}^T, \qquad \boldsymbol{\nu}_2^T = \boldsymbol{\tau}_2^T \wedge \mathbf{n}^T, \qquad \boldsymbol{\nu}_3^T = \boldsymbol{\tau}_3^T \wedge \mathbf{n}^T,$$

we have that the sought approximate density function $\varphi_h \in W_h$ is given by

$$\varphi_h(p) = \sum_{j=1}^{3} \varphi_h(p_{\tau_j}) v_{\tau_j}(p), \quad p \in T, \tag{5.6}$$

where the basis functions are

$$v_{\tau_j}(p) = 1 - \frac{(p - p_{\tau_j}) \cdot \boldsymbol{\nu}_j^T}{h_j^T}, \quad j = 1, 2, 3, \quad p \in T, \tag{5.7}$$

with $h_j = (p_{\tau_i} - p_{\tau_j}) \cdot \boldsymbol{\nu}_j^T > 0$, $i \neq j$. The discrete variational formulation can thus be expressed as follows: Find $\varphi_h \in W_h$ such that

$$\int_\Gamma v_j(p) \left\{ \frac{1}{2}\{\varphi_h(p) - u(p,p)\} + \int_\Gamma \frac{\partial G(p,q)}{\partial \mathbf{n}(q)} \{\varphi_h(q) - \Phi(q,p)\}\, \mathrm{d}s(q) \right.$$
$$\left. - \int_\Gamma v_j(p) G(p,q) \{\mathrm{i}\eta \varphi_h(q) - \Phi_n(q,p)\}\, \mathrm{d}s(q) \right\} \mathrm{d}s(p) = - \int_\Gamma v_j(p) u^{\mathrm{inc}}(p)\, \mathrm{d}s(p) \tag{5.8}$$

for all basis functions $v_j \in W_h$, $j = 1, \ldots, N$.

Consider now the term in (5.8) associated to the single-layer operator, that is,

$$\int_\Gamma v_j(p) \left\{ \int_\Gamma G(p,q) \{\mathrm{i}\eta \varphi_h(q) - \Phi_n(q,p)\}\, \mathrm{d}s(q) \right\} \mathrm{d}s(p)$$
$$= \sum_{T \in \mathcal{T}_h} \sum_{K \in \mathcal{T}_h} \int_T v_j(p) \left\{ \int_K G(p,q) \{\mathrm{i}\eta \varphi_h(q) - \Phi_n(q,p)\}\, \mathrm{d}s(q) \right\} \mathrm{d}s(p). \tag{5.9}$$

Clearly, both the outer and the inner integrals in (5.9) have to be evaluated by means of quadrature rules for which typically the vertices of the triangles $T \in \mathcal{T}_h$ are used as quadrature points. Suppose the vertices p_{τ_ℓ}, $\ell = 1, 2, 3$, are used as quadrature points for evaluation of the outer integral (over T). In order to regularize the integrand of the inner integral (over K), then the normal derivative Φ_n of the planewave interpolant Φ

has to approximate to sufficiently high order the density function $\mathrm{i}\eta\varphi_h$ at the vertices p_{τ_ℓ}, $\ell = 1, 2, 3$. Unfortunately, the problem with this numerical integration scheme is that the construction of Φ requires the surface unit normal and surface tangent vectors to be properly defined at the vertices p_{τ_ℓ}, $\ell = 1, 2, 3$, which does not typically happen for general polyhedral surfaces.

In order to circumvent this issue, we propose to use a second-order Gauss quadrature rule for triangles that makes use of quadrature points $\tilde{p}_\ell$, $\ell = 1, 2, 3$, that lie in the interior T° of the triangle T [11, 15]. This quadrature rule yields the approximation

$$\begin{aligned}\int_T v_j(p)\left\{\int_K G(p,q)\{\mathrm{i}\eta\varphi_h(q) - \Phi_n(q,p)\}\,\mathrm{d}s(q)\right\}\mathrm{d}s(p)\\ \approx \frac{|T|}{3}\sum_{\ell=1}^{3} v_j(\tilde{p}_\ell)\left\{\int_K G(\tilde{p}_\ell,q)\{\mathrm{i}\eta\varphi_h(q) - \Phi_n(q,\tilde{p}_\ell)\}\,\mathrm{d}s(q)\right\},\end{aligned} \tag{5.10}$$

where the quadrature points are given by

$$\tilde{p}_1 = \frac{2p_{\tau_1}}{3} + \frac{p_{\tau_2}}{6} + \frac{p_{\tau_3}}{6},\quad \tilde{p}_2 = \frac{p_{\tau_1}}{6} + \frac{2p_{\tau_2}}{3} + \frac{p_{\tau_3}}{6},\quad \tilde{p}_3 = \frac{p_{\tau_1}}{6} + \frac{p_{\tau_2}}{6} + \frac{2p_{\tau_3}}{3}. \tag{5.11}$$

Since the quadrature points $\tilde{p}_\ell$, $\ell = 1, 2, 3$, lie in the interior of the triangle T (see Figure 1), the surface unit normal and the surface tangent vectors—which are required in the construction of the planewave interpolant—are uniquely defined at those points.

The inner integral, on the other hand, can be approximated by means of any sufficiently high-order quadrature rule. Using the standard node-based quadrature rule, for instance, we obtain

$$\begin{aligned}\int_T v_j(p)\left\{\int_K G(p,q)\{\mathrm{i}\eta\varphi_h(q) - \Phi_n(q,p)\}\,\mathrm{d}s(q)\right\}\mathrm{d}s(p)\\ \approx \frac{|T||K|}{9}\sum_{\ell=1}^{3}\sum_{m=1}^{3} v_j(\tilde{p}_\ell)G(\tilde{p}_\ell,p_{\kappa_m})\{\mathrm{i}\eta\varphi_h(p_{\kappa_m}) - \Phi_n(p_{\kappa_m},\tilde{p}_\ell)\},\end{aligned} \tag{5.12}$$

where p_{κ_m}, $m = 1, 2, 3$, are the vertices of the triangle K (see Figure 1). A completely analogous approach can be followed to evaluate the term in (5.8) involving the double-layer operator.

Remark 5.1. Note that the terms inside the double sum on the right-hand side of (5.12) are always well defined even when the triangles T and K coincide. The effect of the PWDI technique lies then in the regularization of the nearly-singular integral kernels that arise when the triangles T and K coincide or are close to each other. In the latter case, however, the effectiveness of the proposed technique is affected by the limited (piecewise planar) global regularity assumed on the surface parametrization. It is thus not worth pursuing interpolation orders $M \geq 2$ in the context of the proposed BEM for piecewise planar surface representations.

In what follows, we describe in some detail the construction of the closed-form planewave interpolant for $M = 1$ in the Galerkin BEM context. As discussed in section 4.1 above, the construction of the planewave interpolant $\Phi : \mathbb{R}^3 \times \Gamma \to \mathbb{C}$ requires the knowledge of a local smooth parametrization of the surface Γ at and around the interpolation point $p \in \Gamma$. By construction, the interpolation point p always lies in the interior of some triangle $T \in \mathcal{T}_h$. Therefore, the local surface parametrization has constant tangent vectors $\mathbf{e}_1^T$ and $\mathbf{e}_2^T$ that can be computed directly

from the node data. In fact, selecting $\mathbf{e}_1^T = \boldsymbol{\nu}_1^T$ and $\mathbf{e}_2^T = \boldsymbol{\tau}_1^T$, for instance, we have that the expressions for the planewave interpolants (4.6)–(4.7) simplify significantly due to the fact that the metric tensor becomes the identity, i.e., $g_{i,j} = \delta_{i,j}$, and the second fundamental form coefficients vanish, i.e., $L = M = N = 0$, at $p \in T^\circ$.

Having defined the tangent vectors $\mathbf{e}_1^T$ and $\mathbf{e}_2^T$, the surface derivatives of $\varphi_h \in W_h$ at quadrature points $\tilde{p}_\ell \in T^\circ$, $\ell = 1, 2, 3$, can be computed by direct differentiation of (5.6), which in turn involves the derivatives

$$\partial^\alpha v_{\tau_j}(\tilde{p}_\ell) = \begin{cases} \dfrac{1 + 3\delta_{j,\ell}}{6} & \text{if} \quad \alpha = (0,0), \\ -\dfrac{\mathbf{e}_1^T \cdot \boldsymbol{\nu}_j^T}{h_j^T} & \text{if} \quad \alpha = (1,0), \\ -\dfrac{\mathbf{e}_2^T \cdot \boldsymbol{\nu}_j^T}{h_j^T} & \text{if} \quad \alpha = (0,1), \\ 0 & \text{if} \quad |\alpha| > 1 \end{cases} \tag{5.13}$$

of the basis functions (5.7). An algorithmic description of the numerical evaluation of $(v_j, (K - \mathrm{i}\,\eta S)\varphi_h)$ for $j = 1, \ldots, N$ is given in Algorithm 5.2.

Algorithm 5.2. Galerkin BEM evaluation of $(v_j, (K - \mathrm{i}\eta S)\varphi_h)$ for $j = 1, \ldots, N$.

Require: Triangular mesh $\mathcal{T}_h$ of the surface $\Gamma \subset \mathbb{R}^3$ consisting of M triangles and N mesh nodes $\{p_j\}_{j=1}^N \subset \Gamma$; coefficients $\{\varphi_j\}_{j=1}^N \subset \mathbb{C}$ of the density function $\varphi_h(p) = \sum_{j=1}^N \varphi_j v_j(p)$, $p \in \Gamma$, with respect to the basis $\{v_j\}_{j=1}^N$ of piecewise linear polynomials.

Set $I_j = 0$ for all $j = 1, \ldots, N$

for τ from 1 to M **do**

Compute $\mathbf{e}_1^T, \mathbf{e}_2^T, \mathbf{n}^T = \mathbf{e}_1^T \wedge \mathbf{e}_2^T$ and the area $|T|$ of the τth triangle T with vertex indices $\{\tau_1, \tau_2, \tau_3\} \subset \{1, \ldots, N\}$

Produce $\tilde{p}_1, \tilde{p}_1$, and $\tilde{p}_3$ from the vertices p_{τ_1}, p_{τ_2}, and p_{τ_2} using (5.11)

Compute $\partial^\alpha \varphi_h$, $|\alpha| \le M$, at $\tilde{p}_\ell \in T$, $\ell = 1, 2, 3$, using (5.13), to construct the planewave interpolants $\Phi(\cdot, \tilde{p}_\ell)$, $\ell = 1, 2, 3$

for κ from 1 to M **do**

Compute $\mathbf{n}^K$ and the area $|K|$ of the κth mesh triangle K with vertex indices $\{\kappa_1, \kappa_2, \kappa_3\} \subset \{1, \ldots, N\}$

for m from 1 to 3 **do**

Evaluate $F_\ell = f(\tilde{p}_\ell, p_{\kappa_m})$, $\ell = 1, 2, 3$, where $f(p, q) = -\frac{\varphi_h(p)}{2} + \frac{\partial G(p,q)}{\partial \mathbf{n}(q)}\{\varphi_h(q) - \Phi(q, p)\} - G(p, q)\{\mathrm{i}\eta\varphi_h(q) - \Phi_n(q, p)\}$. The normal derivatives $\frac{\partial G(p,q)}{\partial \mathbf{n}(q)}$ and $\Phi_n(q, p) = \frac{\partial \Phi(q,p)}{\partial \mathbf{n}(q)}$ are computed with respect to the unit normal $\mathbf{n}^K$

Update $I_{\tau_1} = I_{\tau_1} + \frac{|T||K|}{9}\{v_{\tau_1}(\tilde{p}_1)F_1 + v_{\tau_1}(\tilde{p}_2)F_2 + v_{\tau_1}(\tilde{p}_3)F_3\}$

Update $I_{\tau_2} = I_{\tau_2} + \frac{|T||K|}{9}\{v_{\tau_2}(\tilde{p}_1)F_1 + v_{\tau_2}(\tilde{p}_2)F_2 + v_{\tau_2}(\tilde{p}_3)F_3\}$

Update $I_{\tau_2} = I_{\tau_3} + \frac{|T||K|}{9}\{v_{\tau_3}(\tilde{p}_1)F_1 + v_{\tau_3}(\tilde{p}_2)F_2 + v_{\tau_3}(\tilde{p}_3)F_3\}$

end for

end for

end for

return I_j for $j = 1, \ldots, N$

In order to tackle the BM integral equation (2.7), in turn we apply the closed-form density interpolation technique to both the single- and the double-layer operators separately. In detail, we first resort to identities (3.15) and (3.17) to express the hypersingular operator in terms of single-layer operators. Then, upon integration by parts, the discrete variational formulation for the BM integral equation reads as follows: Find $\varphi_h \in W_h$ such that

(5.14)
$$\frac{\mathrm{i}\eta}{2}\left(v_j,\varphi_h\right)-\mathrm{i}\eta\left(v_j,K'\varphi_h\right)-\left(\overrightarrow{\operatorname{curl}}_\Gamma v_j,S\overrightarrow{\operatorname{curl}}_\Gamma\varphi_h\right)+k^2\left(v_j\mathbf{n},S\mathbf{n}\varphi_h\right)=-\left(v_j,\frac{\partial u^{\mathrm{inc}}}{\partial\mathbf{n}}\right)$$

for all basis functions $v_j \in W_h$, $j = 1,\dots,N$, where $(\cdot,\cdot)$ denotes the standard real pairing $(\varphi,\psi)=\int_\Gamma \varphi(q)\cdot\psi(q)\,\mathrm{d}s(q)$. Noting that $(v_j,K'\varphi_h)=(Kv_j,\varphi_h)$, we hence conclude that it suffices to apply the proposed technique to both S and K separately (see Remark 3.2).

Finally, in order to produce accurate evaluations of the combined field potential (2.5) at target points $\boldsymbol{r}\in\mathbb{R}^3\setminus\Gamma$ near the surface Γ, we resort once again to the interior quadrature points (5.11). Indeed, in the context of the Galerkin BEM the combined field potential at a point $\boldsymbol{r}\in\mathbb{R}^3\setminus\Gamma$ can be expressed as

(5.15)
$$\begin{aligned}u_D^s(\boldsymbol{r})\approx{}&-\mathbf{1}_\Omega(\boldsymbol{r})\Phi(\boldsymbol{r},p^*)+\sum_{T\in\mathcal{T}_h}\int_T\frac{\partial G(\boldsymbol{r},q)}{\partial\mathbf{n}(q)}\left\{\varphi_h(q)-\Phi(q,p^*)\right\}\mathrm{d}s(q)\\&-\sum_{T\in\mathcal{T}_h}\int_T G(\boldsymbol{r},q)\left\{\mathrm{i}\eta\varphi_h(q)-\Phi_n(q,p^*)\right\}\mathrm{d}s(q)\ \text{with}\ p^*=\arg\min_{q\in\Gamma}|\boldsymbol{r}-q|,\end{aligned}$$

where the integrals over T are approximated as

$$\int_T\frac{\partial G(\boldsymbol{r},q)}{\partial\mathbf{n}(q)}\left\{\varphi_h(q)-\Phi(q,p^*)\right\}\mathrm{d}s(q)\approx\frac{|T|}{3}\sum_{\ell=1}^{3}\frac{\partial G(\boldsymbol{r},\tilde{p}_\ell)}{\partial\mathbf{n}(\tilde{p}_\ell)}\left\{\varphi_h(\tilde{p}_\ell)-u(\tilde{p}_\ell,p^*)\right\},$$

$$\int_T G(\boldsymbol{r},q)\left\{\mathrm{i}\eta\varphi_h(q)-\Phi_n(q,p^*)\right\}\mathrm{d}s(q)\approx\frac{|T|}{3}\sum_{\ell=1}^{3}G(\boldsymbol{r},\tilde{p}_\ell)\left\{\mathrm{i}\eta\varphi_h(\tilde{p}_\ell)-\Phi_n(\tilde{p}_\ell,p^*)\right\}.$$

Remark 5.2. Unless explicitly stated, we follow the standard "$5h$" rule [1] for both the Nyström and the Galerkin BEM versions of the PWDI method. Consequently, fields at a distance smaller than five times the mesh size from the surface are evaluated using the kernel-regularized combined field potential (3.14) (with $p=\arg\min_{q\in\Gamma}|\boldsymbol{r}-q|\in\Gamma$), while fields at target points further away from the surface are computed using the corresponding nonregularized expression (2.5).

6. Numerical examples.

This section presents a variety of numerical experiments that illustrate different aspects of the proposed methodology.

6.1. Validation of the density interpolation procedures.

Our first numerical example is devoted to the validation of the two density interpolation procedures introduced above in section 4. We start off by taking Γ as the (smooth) boundary of the bean-shaped obstacle displayed in Figure 2a, on which we define the density function

$$\rho(q):=\varphi(q)-\Phi(q,p^*),\quad q,p^*\in\Gamma, \tag{6.1}$$

where φ is a given smooth density and Φ is the planewave interpolant at $p^*\in\Gamma$. Note that, by construction, ρ and its first M tangential derivatives vanish at $p^*\in\Gamma$.

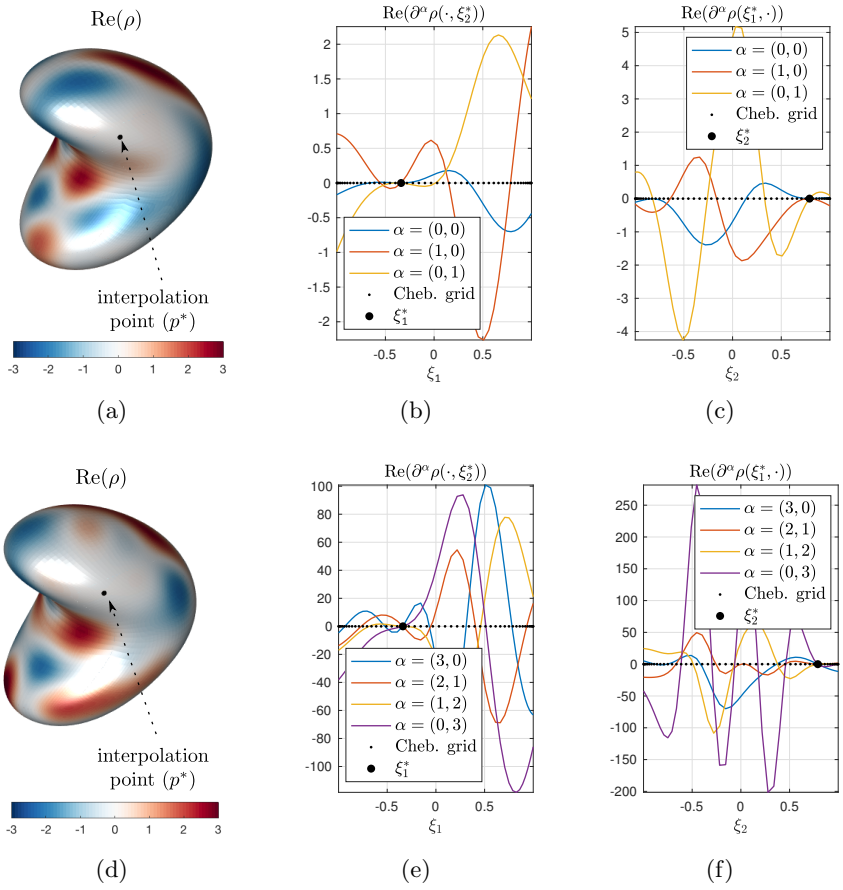

FIG. 2. (a) *(resp.,* (d)*): Plot of the real and imaginary parts of* ρ *defined in* (6.1) *where the planewave interpolant* Φ *was constructed using the analytic (resp., numerical) procedure described in section* 4.1 *(resp.,* 4.2*). The interpolation point* $p^* := \mathbf{x}(\xi_1^*, \xi_2^*) = (-0.616, 0.310, 0.599)$ *is marked by a black dot.* (b) *and* (c) *(resp.,* (e) *and* (f)*): Plots of the cross section of the partial derivatives* $\partial^\alpha \rho$ *for all* $|\alpha| = 1$ *(resp.,* $|\alpha| = 3$*) in the parameter space. Note that all the first- (resp., third-) order derivatives vanish exactly at the interpolation points* $(\xi_1^*, \xi_2^*) = (-0.339, 0.790)$.

As was discussed in section 5.1, the surface Γ is here represented by means of six nonoverlapping rectangular patches, each of which is discretized using Chebyshev grids consisting of 50×50 points. Figure 2a (resp., 2d) displays the real part of ρ produced by the closed-form (resp., algebraic) procedure. Figures 2b and 2c (resp., 2e and 2f), in turn, display slices of the real part of $\partial^\alpha \rho$, $|\alpha| = M$, at p^* in the parameter space, obtained using the closed-form (resp., algebraic) procedure with $M = 1$ (resp., $M = 3$). The density function φ utilized here is selected as the Dirichlet trace of the field produced by a point source at the point $\boldsymbol{r}_0 = (0.1, -0.1, 0.25)$ placed inside Γ. The wavenumber and the coupling parameter considered in this example are $k = 10$ and $\eta = k$, respectively. These results demonstrate that the prescribed Taylor interpolation order M is achieved by the proposed procedures. Similar results are obtained for the imaginary part of ρ as well as for $\rho_n(q) = \mathrm{i}\eta\varphi(q) - \Phi_n(q, p^*)$, which, for the sake of brevity, are not displayed here.

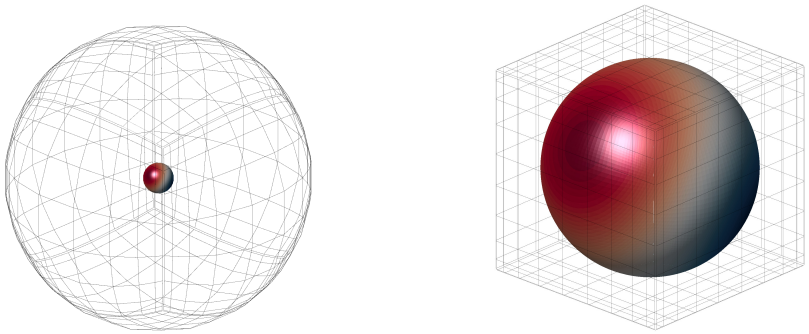

(a) Far-field evaluation grid (b) Near-field evaluation grid

FIG. 3. *Grids utilized in the evaluation of the far- and near-field errors.*

6.2. Nyström and Galerkin boundary element methods. This section illustrates the capabilities of the density interpolation method for the regularization of the combined field potential and the associated BW and BM integral operators.

6.2.1. Simple surfaces. In our first example, we let Γ be a unit sphere at the origin. (This simple surface has the advantage that can be easily represented using both quadrilateral patches and triangular meshes, allowing us to tackle the same problems using both Nyström methods and Galerkin BEMs.) In order to assess the numerical errors, we consider an exact solution for both Dirichlet (2.1) and Neumann (2.2) problems, which is given by $u^s_{\text{exact}}(\boldsymbol{r}) = \mathrm{e}^{\mathrm{i}k|\boldsymbol{r}-\boldsymbol{r}_0|}/|\boldsymbol{r}-\boldsymbol{r}_0| - \mathrm{e}^{\mathrm{i}k|\boldsymbol{r}-\boldsymbol{r}_1|}/|\boldsymbol{r}-\boldsymbol{r}_1|$, where the source points $\boldsymbol{r}_0 = (0.2, 0.1, 0.1)$ and $\boldsymbol{r}_1 = (-0.1, 0.3, -0.1)$ lie inside the unit sphere Γ. The real part of the Dirichlet trace of u^s_{exact} on Γ (for $k = 1$) is plotted (in colors) in Figures 3a and 3b. The far-field errors in the numerical solution u^s are measured by

$$\text{Error} = \frac{\max_{\boldsymbol{r}\in\Xi} |u^s_{\text{exact}}(\boldsymbol{r}) - u^s(\boldsymbol{r})|}{\max_{\boldsymbol{r}\in\Xi} |u^s_{\text{exact}}(\boldsymbol{r})|}, \tag{6.2}$$

where Ξ is the spherical grid (of radius $r = 10$) displayed in Figure 3a. The near-field errors, in turn, are measured using (6.2) but with Ξ being the grid of the cube of side length two displayed in Figure 3b. Note that Γ touches the cube surface grid at the center of its six faces.

The accuracy of the Chebyshev-based Nyström method is assessed first. Figures 4a and 4b display the far- and near-field errors, respectively, in the approximate Dirichlet solution obtained from the kernel-regularized BW integral equation (3.11) for $k = \eta = 1$. These figures display the errors obtained using the (closed-form) analytical (A-PWDI) procedure as well as the (algebraic) numerical (N-PWDI) density interpolation procedure introduced in sections 4.1 and 4.2, respectively, for various discretization sizes N and density interpolation orders M. The surface Γ is here represented using six quadrilateral patches, and each one of them is discretized using a Chebyshev grid of $N \times N$ points. The near fields were computed using the kernel-regularized combined field potential (3.10), while the far fields were, in turn, computed using the nonregularized expression (2.5). We note here that the slightly larger errors produced by the N-PWDI procedure for $M = 0$ and 1 can be attributed to the ill-conditioning of the matrix $\boldsymbol{C}(p)\boldsymbol{C}^*(p)$ that is inverted to generate the planewave coefficients in the case of the N-PWDI. Results closer to the ones produced

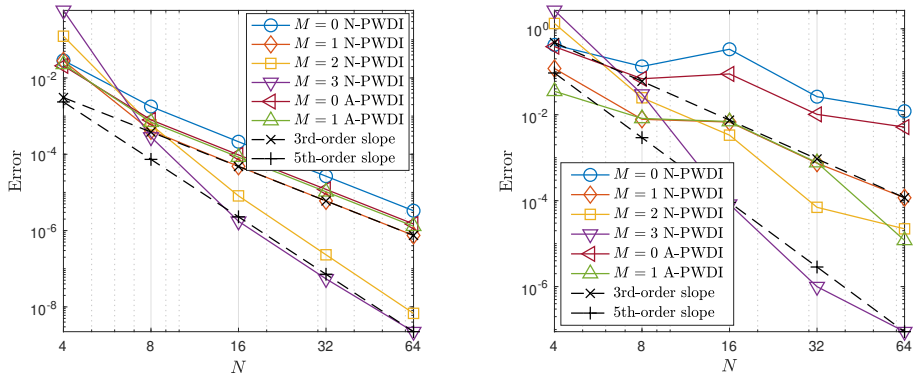

(a) Far-field (relative) errors

(b) Near-field (relative) errors

FIG. 4. *Far- and near-field errors in the solution of the Dirichlet problem* (2.1) *produced by the Nyström method discretization of the BW integral equation* (2.6) *using the two proposed PWDI techniques for different interpolation orders M and grid sizes N (each quadrilateral surface patch is discretized using $N \times N$ quadrature points).*

by the A-PWDI can be obtained by increasing the number of planewave directions L used in the construction of the density interpolant (see Remark 4.3).

As can be observed in these results, the proposed technique yields third-order convergence of the far fields (as the grid size N increases) for interpolation orders $M = 0$ and 1 and fifth-order convergence for $M = 2$ and 3. In the near field, on the other hand, third-order convergence is observed for all orders, with the only exception of $M = 3$, for which fifth order is achieved as N increases. It is worth mentioning that the associated linear systems were solved iteratively by means of GMRES [32] with an error tolerance of 10^{-8}. A nearly constant number of iterations ($\sim$10) was needed in all the examples considered in Figure 4. As in the case of the Laplace equation in two dimensions using the trapezoidal rule [30, Remark 6.1], the fact that the interpolation orders $M = 0$ and 1, and also $M = 2$ and 3, render the same order of convergence can be explained by the fact that Fejér's quadrature rule in this case integrates certain odd singular terms exactly.

The geometric setup of Figure 3 is next used to assess the accuracy of the Chebyshev-based Nyström method when dealing with the more challenging BM integral equation (2.7) for the solution of the Neumann problem (2.2). The relevant numerical results are summarized in Table 1, where it can be clearly seen that, despite the overall smaller errors obtained for $M = 3$, both interpolation orders $M = 2$ and $M = 3$ yield far- and near-field errors that exhibit the same nearly third-order convergence rate as N increases. As in the previous example, the near fields were computed using the kernel-regularized combined field potential (3.10), while the far fields were, in turn, computed using the nonregularized expression (2.5). Directly-regularized (3.14) and Maue-regularized (3.16) versions of the hypersingular operator were considered in these examples. A number of GMRES iterations as large as 200 was needed to achieve the desired accuracy in some of the examples considered in Table 1 due to the known unfavorable spectral properties of the hypersingular operator present in the BM integral equation. As is well known, the number of GMRES iterations can be drastically reduced by considering appropriate preconditioners for the hypersingular operator (cf. [2, 4]).

TABLE 1

Far- and near-field errors in the solution of the Neumann problem (2.2) *produced by the Nyström discretization of the BM integral equation* (2.7) *using the numerical PWDI procedure of section* 4.2 *for* $M = 2, 3$ *and various grid sizes* N.

Nyström method — BM integral equation

N	$M = 2$		$M = 3$	
	Directly-regularized	Maue-regularized	Directly-regularized	Maue-regularized
	Far-field			
4	$8.55 \cdot 10^{-2}$	$2.01 \cdot 10^{-1}$	$8.89 \cdot 10^{-2}$	$6.66 \cdot 10^{-2}$
8	$1.73 \cdot 10^{-3}$	$8.44 \cdot 10^{-3}$	$3.55 \cdot 10^{-4}$	$2.03 \cdot 10^{-3}$
16	$3.46 \cdot 10^{-4}$	$9.46 \cdot 10^{-4}$	$5.31 \cdot 10^{-5}$	$2.60 \cdot 10^{-4}$
32	$4.13 \cdot 10^{-5}$	$1.21 \cdot 10^{-4}$	$7.22 \cdot 10^{-6}$	$3.22 \cdot 10^{-5}$
	Near-field			
4	$1.61 \cdot 10^{-0}$	$9.37 \cdot 10^{-1}$	$1.19 \cdot 10^{-0}$	$2.48 \cdot 10^{-0}$
8	$7.32 \cdot 10^{-3}$	$1.63 \cdot 10^{-2}$	$3.31 \cdot 10^{-3}$	$6.72 \cdot 10^{-3}$
16	$1.86 \cdot 10^{-3}$	$1.53 \cdot 10^{-3}$	$1.79 \cdot 10^{-4}$	$8.35 \cdot 10^{-4}$
32	$2.27 \cdot 10^{-5}$	$2.02 \cdot 10^{-4}$	$2.08 \cdot 10^{-5}$	$8.29 \cdot 10^{-5}$

We next consider once again the Dirichlet and Neumann problems posed in the exterior of the unit sphere but now utilizing Galerkin BEM discretizations of the associated BW (2.6) and BM (2.7) integral equations. The numerical results are summarized in Table 2. The closed-form analytical density interpolation procedure of section 5.2 is used in all the examples included in this table. The discrete variational formulations corresponding to the BW and BM integral equations are given in (5.8) and (5.14), respectively. We recall that the latter is here discretized as indicated in section 5.2—by expressing it in terms of kernel-regularized single- and double-layer operators. The near fields in this case were computed using the kernel-regularized combined field potential (5.15), while the far fields were computed as before using the nonregularized expression (2.5). As expected, these results demonstrate that far-field errors exhibit second-order convergence rates for both BIEs and interpolation orders $M = 0$ and 1 as the mesh size $h = \max_{T \in \mathcal{T}_h, i,j=1,2,3} |p_{\tau_i} - p_{\tau_j}|$ decreases. In fact, the errors obtained using the interpolation orders $M = 0$ and 1 are almost identical. The closeness of the errors observed might be explained by the possible dominance of the Galerkin-BEM $\mathcal{O}(h^2)$ errors over the errors introduced by the numerical integration procedure. The near-field errors, on the other hand, exhibit nearly second-order convergence rates for both orders $M = 0$ and 1, with significantly smaller errors obtained for $M = 1$.

6.2.2. More complex surfaces. In order to demonstrate the accuracy of the Nyström method when dealing with more complex geometries, we consider the scattering of a planewave $u^{\text{inc}}(\boldsymbol{r}) = \mathrm{e}^{\mathrm{i}k\boldsymbol{r}\cdot\boldsymbol{d}}$, in the direction $\boldsymbol{d} = (\cos\frac{\pi}{3}, -\sin\frac{\pi}{3}, 0)$, that impinges on the three sound-soft obstacles shown in Figure 5. The resulting scattered field is the solution of the exterior Dirichlet problem (2.1) that is here solved by means of the Nyström method applied to the kernel-regularized BW integral equation (3.11). The far-field errors reported in Figure 5 were produced by (6.2) with the set Ξ being the spherical grid displayed in Figure 3a. The reference solution u^s_{exact} in (6.2) was generated using a fine discretization of the BW integral equation consisting of Chebyshev grids comprising 36×36 points per surface patch. Both (algebraic) numerical (with $M = 2$) and (closed-form) analytical (with $M = 1$) density inter-

TABLE 2

Far- and near-field relative errors in the solution of the Dirichlet problem (2.1) *produced by the boundary element discretization of the BW integral equation* (2.6) *using the analytical PWDI technique for different interpolation orders M and mesh sizes h. The surface Γ considered in this example is a sphere of unit radius and centered at the origin.*

Galerkin BEM

h	DoF	Far-field		Near-field	
		$M = 0$	$M = 1$	$M = 0$	$M = 1$
		BW integral equation			

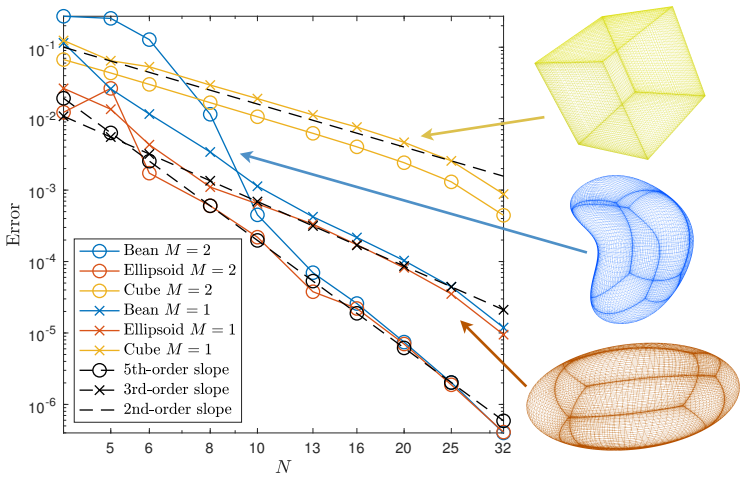

FIG. 5. *Far-field errors in the solution of the Dirichlet problem* (2.1) *corresponding to the scattering of a planewave off three different surfaces using the Chebyshev-based Nyström method of section* 5.1 *applied to the BW integral equation* (2.6) *with $k = \eta = 1$. Both analytical (with $M = 1$) and numerical (with $M = 2$) PWDI procedures were used in this example.*

polation procedures are utilized in this example. Third- and fifth-order convergence rates of the far-field errors are observed for $M = 1$ and 2, respectively, for the smooth surface cases (bean and ellipsoid). Only second-order convergence is achieved in the nonsmooth surface case (cube) for both interpolation orders $M = 1$ and 2. The poor convergence rate observed in the latter case is explained by the singular behavior of the integral equation solution φ along the edges of the cube (cf. [10]). In fact, for the interior point source problem described above in this section—in which case φ is smooth up to the edges of the cube—third- and fifth-order convergence rates are attained. The total field solution of a higher-frequency scattering problem for the bean-shaped obstacle—whose diameter is 10λ ($k = 2\pi/\lambda = 10\pi$)—is shown in Fig-

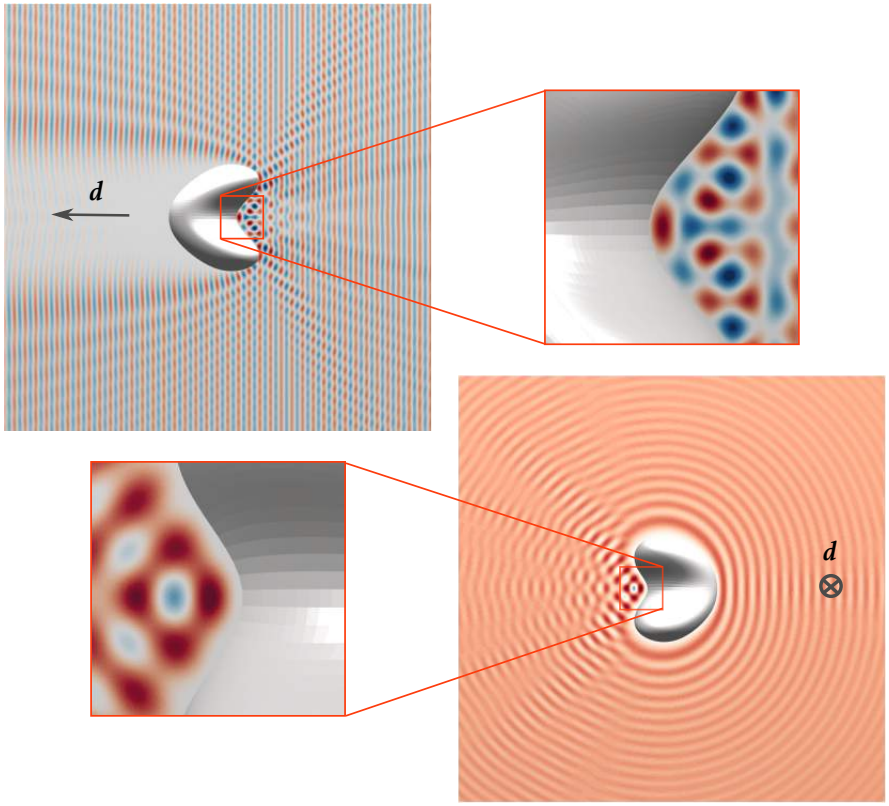

FIG. 6. *Real part of the total field* $u = u_D^{\mathrm{s}} + u^{\mathrm{inc}}$, *where* u_D^{s} *is the solution of the exterior Dirichlet problem* (2.1) *corresponding to the scattering of the planewave* $u^{\mathrm{inc}}(\boldsymbol{r}) = \mathrm{e}^{\mathrm{i}k\boldsymbol{r}\cdot\boldsymbol{d}}$, *with* $k = 10\pi$ *and* $\boldsymbol{d} = (\cos\pi/3, -\sin\pi/3, 0)$, *off of a bean-shaped obstacle. Top: total field at a plane parallel to* $\boldsymbol{d}$ *that passes through the center of the obstacle. Bottom: total field at a plane perpendicular to* $\boldsymbol{d}$ *that passes through the center of the obstacle. The surface* Γ *was discretized using six* 48×48 *Chebyshev grids. The discretized BW integral equation (with* $\eta = k$*) was solved by means of GMRES, which required* 55 *iterations to attain the prescribed* 10^{-7} *error tolerance.*

ure 6. The near fields displayed in Figure 6 are accurate to at least four decimal places everywhere, including near and on the surface of the bean obstacle.

To finalize this section, we present examples aiming at demonstrating the capability of the BEM solver of handling complex geometries of engineering relevance. To this end, we consider a triangular mesh representation of a Falcon airplane produced by Gmsh [16], which is used in the solution of two Dirichlet problems (2.1) with different incident fields. In the first example, we validate our BEM solver for this challenging geometry by considering an incident field given by two point sources placed inside the airplane's fuselage. The numerical solution is then compared with the exact solution. For the wavenumber $k = 0.5\pi$ and the mesh size $h = 1.62$, we obtain a relative error (6.2) of $8.1 \cdot 10^{-2}$ at a sphere containing the airplane. The near-field error at two different planes intersecting the airplane is displayed in the first row of Figure 7. Finally, our second example considers a planewave incident field in the direction $\boldsymbol{d} = (\cos\frac{\pi}{4}, -\sin\frac{\pi}{4}, 0)$ for the same wavenumber ($k = 0.5\pi$). Two views of the real part of the total field are displayed in the second row of Figure 7, where the acoustic shadow can be clearly seen under the airplane.

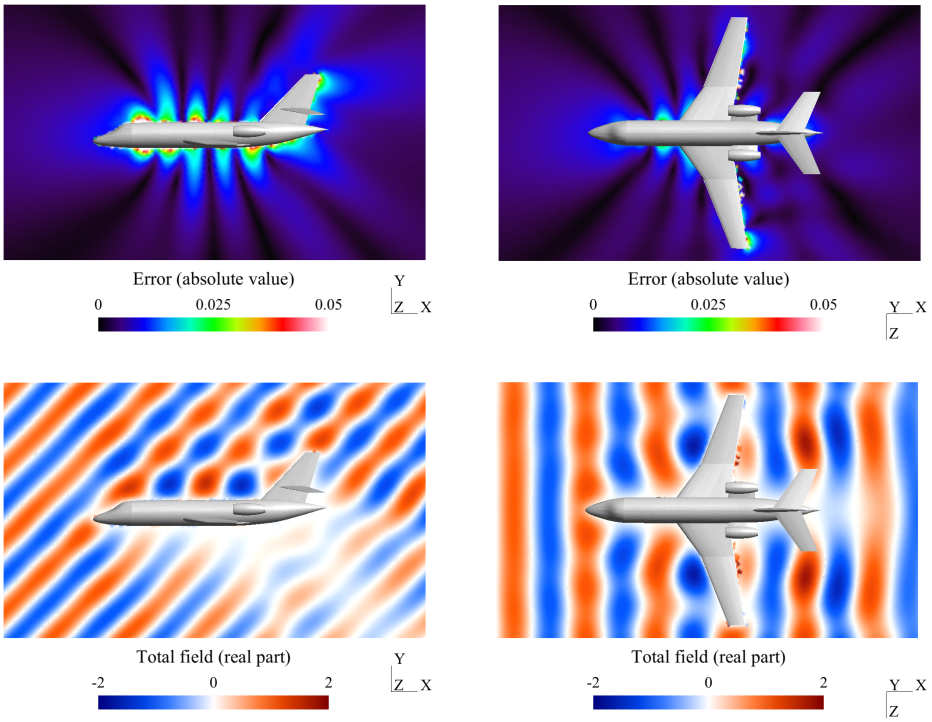

FIG. 7. *First row: Two views of the absolute error in the Galerkin BEM solution of* (2.1) *with* $k = 0.5\pi$ *for an incident field corresponding to two point sources placed inside the surface* Γ *which models a Falcon airplane. The relative error* (6.2) *on a sphere containing the airplane is* $8.1 \cdot 10^{-2}$ *in this example, where the mesh size is* $h = 1.62$. *Second row: Two views of the real part of the total field solution of the problem of scattering* (2.1) *for a planewave incident field in the direction* $\boldsymbol{d} = (\cos\frac{\pi}{4}, -\sin\frac{\pi}{4}, 0)$. *The analytical PWDI procedure with* $M = 1$ *was used in all these examples.*

6.2.3. Composite surfaces. In this final section, we apply the approach put forth in section 3.3 to the solution of the Dirichlet problem (2.1), posed in the exterior of the composite domain $\Omega = \Omega_1 \cup \Omega_2$ with boundary $\Gamma = \partial(\Omega_1 \cup \Omega_2)$, where Ω_1 is a sphere of radius 0.5 and Ω_2 is a hemisphere of radius 1.5. The incident field used in this example is a planewave $u^{\text{inc}}(\boldsymbol{r}) = \mathrm{e}^{\mathrm{i}\, k\boldsymbol{d}\cdot\boldsymbol{r}}$ in the direction $\boldsymbol{d} = (\cos\frac{\pi}{4}, 0, -\sin\frac{\pi}{4})$ and $k = \eta = 1$. The multiple-scattering BW integral equation (3.18), posed on $\tilde{\Gamma} = \partial\Omega_1 \cup \partial\Omega_2$, is discretized using the BEM detailed in section 5.2 with $M = 1$. Figure 8 presents the far-field errors for various mesh sizes h. The error is defined here as in (6.2) with Ξ being the spherical grid shown in Figure 3a and the reference solution u^s_{exact} being produced using a fine mesh discretization, with $h = 0.11$, of the surfaces Γ_1 and Γ_2. Three different Ω configurations, shown in inset plots in Figure 8, are considered, including one (on the left-hand side) in which the two obstacles are touching at a single point. Clearly, second-order convergence is achieved, as h decreases, in all three configurations. The real part of the total field solution of the problem of scattering (for $k = \eta = 5$), together with the absolute value of the error obtained using the multiple-scattering approach and the standard approach, is shown in Figure 9. The reference solution for the error estimation is produced using a fine-grid discretization of Γ using $h = 0.1$.

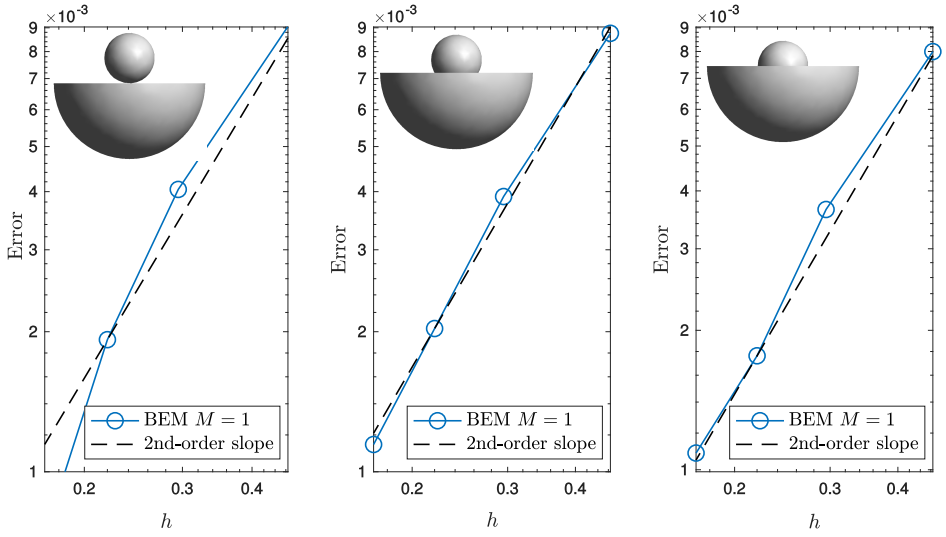

FIG. 8. *Far-field errors in the solution of the Dirichlet problem* (2.1) *corresponding to the scattering of a planewave in the direction* $\boldsymbol{d} = (\cos\frac{\pi}{4}, 0, -\sin\frac{\pi}{4})$ *off of three different composite structures using the Galerkin BEM presented in section* 5.1 *applied to the BW integral equation* (2.6) *with* $k = \eta = 1$. *The analytical PWDI procedure with* $M = 1$ *was used in this example. Separate meshes of the sphere and the hemisphere were used in this example.*

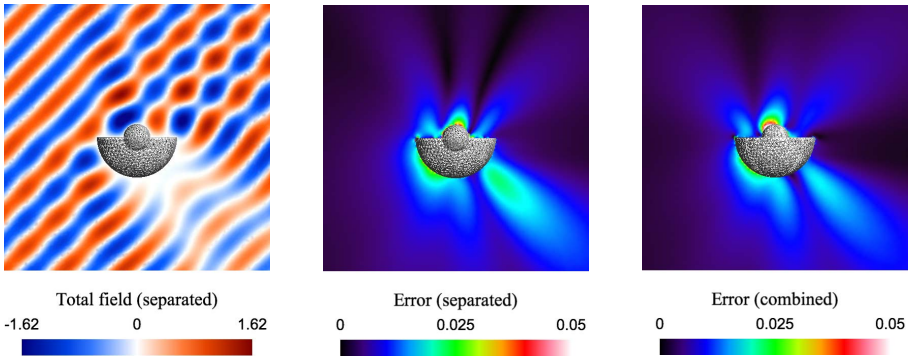

FIG. 9. *Left: total near field corresponding to the scattering of a planewave in the direction* $\boldsymbol{d} = (\cos\frac{\pi}{4}, 0, -\sin\frac{\pi}{4})$ *using the Galerkin BEM presented in section* 5.1 *applied to the BW integral equation* (2.6) *with* $k = \eta = 4$ *using separated meshes for the upper sphere and lower hemisphere. Center: error in the solution using separated meshes with* $h = 0.22$. *Right: error in the solution using a combined mesh with* $h = 0.21$. *Reference solution computed using a combined mesh with* $h = 0.1$. *The analytical PWDI procedure with* $M = 1$ *was used in this example.*

Remark 6.1. Finally, we recall that the proposed regularization procedure for the evaluation of the potential (3.10) and the multiple scattering operators of section 3.3 involves computing the distance from a given target point $\boldsymbol{r} \in \mathbb{R}^3 \setminus \Gamma$ to the surface and finding its closest point $p^* \in \Gamma$. In the numerical examples presented in section 6 above, these tasks were performed by means of a naive and rather expensive procedure that consists in computing the distances from the target point $\boldsymbol{r}$ to every discretization point p on the integration surface Γ. For N_t target points, this procedure entails

an overall computational cost of $\mathcal{O}(N_t N)$, where N is the total number of discretization points on Γ. This computational cost, however, can be significantly reduced by introducing a hierarchical partition of the space containing the surface Γ, which can at the same time be utilized to accelerate the linear system solution by means of the fast multipole method [18] or $\mathcal{H}$-matrix compression [19]. In fact, having an octree data structure enables the use of efficient algorithms that reduce the computational cost of computing the distance and finding the closest point to $\mathcal{O}(\log N)$ operations per target point, thus reducing the overall cost to $\mathcal{O}(N_t \log N)$ operations. This and other issues concerning a fast version of the PWDI method will be addressed in a future contribution.

REFERENCES

[1] A. H. Barnett, *Evaluation of layer potentials close to the boundary for Laplace and Helmholtz problems on analytic planar domains*, SIAM J. Sci. Comput., 36 (2014), pp. A427–A451, https://doi.org/10.1137/120900253.

[2] Y. Boubendir and C. Turc, *Wave-number estimates for regularized combined field boundary integral operators in acoustic scattering problems with Neumann boundary conditions*, IMA J. Numer. Anal., 33 (2013), pp. 1176–1225.

[3] H. Brakhage and P. Werner, *Über das dirichletsche aussenraumproblem für die Helmholtzsche schwingungsgleichung*, Arch. Math., 16 (1965), pp. 325–329.

[4] O. P. Bruno, T. Elling, and C. Turc, *Regularized integral equations and fast high-order solvers for sound-hard acoustic scattering problems*, Internat. J. Numer. Methods Engrg., 91 (2012), pp. 1045–1072.

[5] O. P. Bruno and L. A. Kunyansky, *A fast, high-order algorithm for the solution of surface scattering problems: Basic implementation, tests, and applications*, J. Comput. Phys., 1 (2001), pp. 80–110.

[6] A. Burton and G. Miller, *The application of integral equation methods to the numerical solution of some exterior boundary-value problems*, Proc. Roy. Soc. London Ser. A, 323 (1971), pp. 201–210.

[7] S. Caorsi, D. Moreno, and F. Sidoti, *Theoretical and numerical treatment of surface integrals involving the free-space Green's function*, IEEE Trans. Antennas and Propagation, 41 (1993), pp. 1296–1301.

[8] M. Chen and B. Lu, *TMSmesh: A robust method for molecular surface mesh generation using a trace technique*, J. Chem. Theory Comput., 7 (2010), pp. 203–212.

[9] D. L. Colton and R. Kress, *Integral Equation Methods in Scattering Theory*, 1st ed., Pure Appl. Math. (N. Y.), John Wiley & Sons, New York, 1983.

[10] M. Costabel and M. Dauge, *Singularities of electromagnetic fields in polyhedral domains*, Arch. Ration. Mech. Anal., 151 (2000), pp. 221–276.

[11] G. Cowper, *Gaussian quadrature formulas for triangles*, Internat. J. Numer. Methods Engrg., 7 (1973), pp. 405–408.

[12] P. J. Davis and P. Rabinowitz, *Methods of Numerical Integration*, Dover, New York, 2007.

[13] M. P. do Carmo, *Differential Geometry of Curves and Surfaces*, revised and updated 2nd ed., Dover, New York, 2016.

[14] M. G. Duffy, *Quadrature over a pyramid or cube of integrands with a singularity at a vertex*, SIAM J. Numer. Anal., 19 (1982), pp. 1260–1262, https://doi.org/10.1137/0719090.

[15] D. Dunavant, *High degree efficient symmetrical Gaussian quadrature rules for the triangle*, Internat. J. Numer. Methods Engrg., 21 (1985), pp. 1129–1148.

[16] C. Geuzaine and J.-F. Remacle, *Gmsh: A 3-D finite element mesh generator with built-in pre-and post-processing facilities*, Internat. J. Numer. Methods Engrg., 79 (2009), pp. 1309–1331.

[17] R. D. Graglia, *On the numerical integration of the linear shape functions times the 3-D Green's function or its gradient on a plane triangle*, IEEE Trans. Antennas and Propagation, 41 (1993), pp. 1448–1455.

[18] L. Greengard, J. Huang, V. Rokhlin, and S. Wandzura, *Accelerating fast multipole methods for the Helmholtz equation at low frequencies*, IEEE Comput. Sci. Eng., 5 (1998), pp. 32–38.

[19] W. Hackbusch, *Hierarchical Matrices: Algorithms and Analysis*, Springer, Heidelberg, 2015.

[20] W. Hackbusch and S. A. Sauter, *On the efficient use of the Galerkin-method to solve Fred-*

holm integral equations, Appl. Math., 38 (1993), pp. 301–322.
[21] W. Hackbusch and S. A. Sauter, *On numerical cubatures of nearly singular surface integrals arising in BEM collocation*, Computing, 52 (1994), pp. 139–159.
[22] S. Järvenpää, M. Taskinen, and P. Ylä-Oijala, *Singularity extraction technique for integral equation methods with higher order basis functions on plane triangles and tetrahedra*, Internat. J. Numer. Methods Engrg., 58 (2003), pp. 1149–1165.
[23] S. Jarvenpaa, M. Taskinen, and P. Yla-Oijala, *Singularity subtraction technique for high-order polynomial vector basis functions on planar triangles*, IEEE Trans. Antennas and Propagation, 54 (2006), pp. 42–49.
[24] E. Klaseboer, Q. Sun, and D. Y. C. Chan, *Non-singular boundary integral methods for fluid mechanics applications*, J. Fluid Mech., 696 (2012), pp. 468–478.
[25] Y. Liu and T. Rudolphi, *Some identities for fundamental solutions and their applications to weakly-singular boundary element formulations*, Eng. Anal. Bound. Elem., 8 (1991), pp. 301–311.
[26] Y. Liu and T. Rudolphi, *New identities for fundamental solutions and their applications to non-singular boundary element formulations*, Comput. Mech., 24 (1999), pp. 286–292.
[27] W. C. H. McLean, *Strongly Elliptic Systems and Boundary Integral Equations*, Cambridge University Press, Cambridge, UK, 2000.
[28] J.-C. Nédélec, *Acoustic and Electromagnetic Equations: Integral Representations for Harmonic Problems*, Appl. Math. Sci. 144, Springer, New York, 2001.
[29] C. Pérez-Arancibia, *A plane-wave singularity subtraction technique for the classical Dirichlet and Neumann combined field integral equations*, Appl. Numer. Math., 123 (2018), pp. 221–240.
[30] C. Pérez-Arancibia, L. Faria, and C. Turc, *Harmonic density interpolation methods for high-order evaluation of Laplace layer potentials in 2D and 3D*, J. Comput. Phys., 376 (2019), pp. 411–434.
[31] M. H. Reid, J. K. White, and S. G. Johnson, *Generalized Taylor–Duffy method for efficient evaluation of Galerkin integrals in boundary-element method computations*, IEEE Trans. Antennas and Propagation, 63 (2015), pp. 195–209.
[32] Y. Saad and M. H. Schultz, *GMRES: A generalized minimal residual algorithm for solving nonsymmetric linear systems*, SIAM J. Sci. Statist. Comput., 7 (1986), pp. 856–869, https://doi.org/10.1137/0907058.
[33] S. A. Sauter, *Cubature techniques for 3-D Galerkin BEM*, in Boundary Elements: Implementation and Analysis of Advanced Algorithms, Vieweg+Teubner Verlag, Wiesbaden, 1996, pp. 29–44.
[34] S. A. Sauter and C. Lage, *Transformation of hypersingular integrals and black-box cubature*, Math. Comp., 70 (2001), pp. 223–250.
[35] H. Schulz, C. Schwab, and W. L. Wendland, *The computation of potentials near and on the boundary by an extraction technique for boundary element methods*, Comput. Methods Appl. Mech. Engrg., 157 (1998), pp. 225–238.
[36] C. Schwab and W. L. Wendland, *On numerical cubatures of singular surface integrals in boundary element methods*, Numer. Math., 62 (1992), pp. 343–369.
[37] C. Schwab and W. L. Wendland, *On the extraction technique in boundary integral equations*, Math. Comp., 68 (1999), pp. 91–123.
[38] Q. Sun, E. Klaseboer, B. C. Khoo, and D. Y. Chan, *A robust and non-singular formulation of the boundary integral method for the potential problem*, Eng. Anal. Bound. Elem., 43 (2014), pp. 117–123.
[39] Q. Sun, E. Klaseboer, B.-C. Khoo, and D. Y. Chan, *Boundary regularized integral equation formulation of the Helmholtz equation in acoustics*, R. Soc. Open Sci., 2 (2015), 140520.
[40] D. Wilton, S. Rao, A. Glisson, D. Schaubert, O. Al-Bundak, and C. Butler, *Potential integrals for uniform and linear source distributions on polygonal and polyhedral domains*, IEEE Trans. Antennas and Propagation, 32 (1984), pp. 276–281.
[41] P. Yla-Oijala and M. Taskinen, *Calculation of CFIE impedance matrix elements with RWG and $n\times$RWG functions*, IEEE Trans. Antennas and Propagation, 51 (2003), pp. 1837–1846.